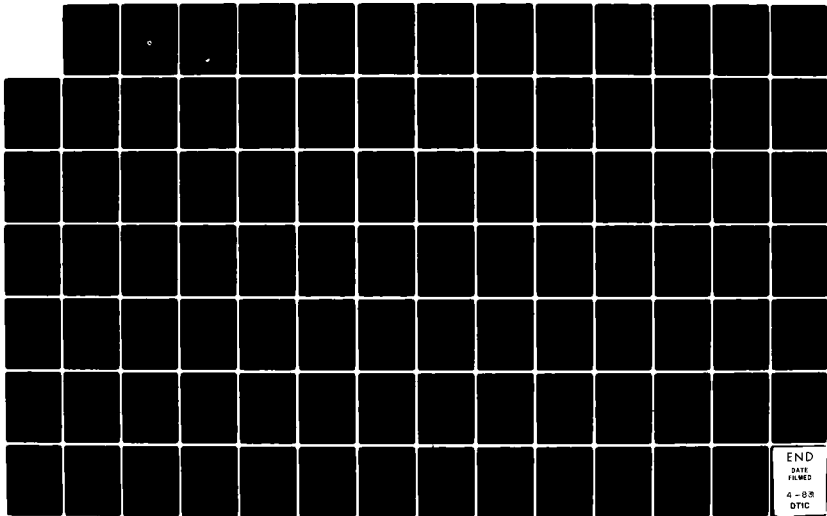AD-A126 316   MODELING SEA ICE TRAJECTORIES FOR OIL SPILL TRACKING   1/1
             (U) FLOW RESEARCH CO KENT WA   R S PRITCHARD ET AL.
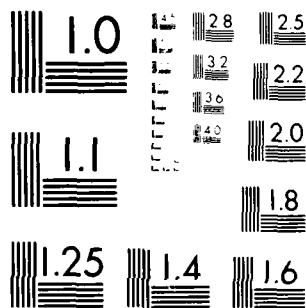   JUN 81 FRC-187 USCG-D-28-81 DTCG39-80-C-80091

UNCLASSIFIED   F/G 12/1   NL

END
DATE
FILMED
4-83
DTIC

MICROCOPY RESOLUTION TEST CHART

NATIONAL BUREAU OF STANDARDS-1963-A

AD A126316

MODELING SEA ICE TRAJECTORIES
FOR
OIL SPILL TRACKING

R. S. Pritchard
J. J. Kollé

Flow Research Company

21414-68th Avenue South

Kent, Washington 98031

JUNE 1981

FINAL REPORT

Prepared for

U.S. DEPARTMENT OF TRANSPORTATION
UNITED STATES COAST GUARD
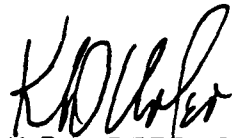**Office of Research and Development**
Washington, D.C. 20590

N O T I C E

This document is disseminated under the sponsorship of the
Department of Transportation in the interest of information
exchange. The United States Government assumes no liability
for its contents or use thereof.

The United States Government does not endorse products or
manufacturers. Trade or manufacturers' names appear herein
soley because they are considered essential to the object of
this report.

The contents of this report reflect the views of the Coast
Guard Research and Development Center, which is responsible
for the facts and accuracy of data presented. This report
does not constitute a standard , specification, or regulation.

K.D. URFER, CAPT., USCG
Commanding Officer
U.S. Coast Guard Research and Development Center
Avery Point, Groton, Connecticut 06340

1. Report No.	2. Government Accession No.	3. Recipient's Catalog No
CG-D-28-81	AD A126 316	

4. Title and Subtitle	5. Report Date
MODELING SEA ICE TRAJECTORIES FOR OIL SPILL TRACKING	June 1981
	6. Performing Organization Code

7. Author(s)	8. Performing Organization Report No
R. S. Pritchard and J. J. Kollé	FRC Report No. 187

9. Performing Organization Name and Address	10. Work Unit No. (TRAIS)
Flow Research Company	
21414 - 68th Ave. South	11. Contract or Grant No
Kent, WA 98031	DTCG39-80-C-80091
	13. Type of Report and Period Covered

12. Sponsoring Agency Name and Address	
U.S. Department of Transportation	Final Report
United States Coast Guard	1 Aug 1980 - 31 Mar 1981
Office of Research and Development	14. Sponsoring Agency Code
Washington, D.C. 20590	

15. Supplementary Notes

The contract under which this report was submitted was under the technical supervision of the Coast Guard Research and Development Center, Groton, Connecticut. R&D Center number CGR/DC 10/81 has been assigned

16. Abstract

A free-drift ice model and a complete sea ice dynamics model are presented and used for simulating trajectories of Arctic sea ice. The development of these models is part of a U.S. Coast Guard study to provide methods for predicting the movement of oil spills in Arctic and sub-Arctic coastal waters. Performance of both models is compared with sea ice motions observed during the AIDJEX main field experiment in the Beaufort Sea from April 1975 to February 1976. The average error in the free-drift model during the summer is 0.010 m/s with a standard deviation of 0.030 m/s while the more complete model gives an error of 0.005 m/s with a standard deviation of 0.020 m/s. The complete ice dynamics model is almost as accurate during the winter (0.005 m/s mean error, 0.036 m/s standard deviation) but the free-drift model performance degrades substantially (0.030 m/s mean error and 0.107 m/s standard deviation). Therefore, both models are useful tools for simulating and predicting summertime ice motions on the Beaufort Sea but only the complete ice dynamics model can accurately describe wintertime ice behavior.

17. Key Words	18. Distribution Statement
oil spills, AIDJEX, Beaufort Sea, free-drift, ice cover modeling, ice trajectories, sea ice dynamics, sea ice statistics	Document is available to the U.S. public through the National Technical Information Service, Springfield, Virginia 22161.

19. Security Classif. (of this report)	20. Security Classif. (of this page)	21. No. of Pages	22. Price
UNCLASSIFIED	UNCLASSIFIED	85	

Form DOT F 1700.7 (8-72) Reproduction of completed page authorized

i

METRIC CONVERSION FACTORS

Approximate Conversions to Metric Measures

Symbol	When You Know	Multiply By	To Find	Symbol
	LENGTH			
in	inches	* 2.5	centimeters	cm
ft	feet	30	centimeters	cm
yd	yards	0.9	meters	m
mi	miles	1.6	kilometers	km
	AREA			
in²	square inches	6.5	square centimeters	cm²
ft²	square feet	0.09	square meters	m²
yd²	square yards	0.8	square meters	m²
mi²	square miles	2.6	square kilometers	km²
	acres	0.4	hectares	ha
	MASS (WEIGHT)			
oz	ounces	28	grams	g
lb	pounds	0.45	kilograms	kg
	short tons (2000 lb)	0.9	tonnes	t
	VOLUME			
tsp	teaspoons	5	milliliters	ml
tbsp	tablespoons	15	milliliters	ml
fl oz	fluid ounces	30	milliliters	ml
c	cups	0.24	liters	l
pt	pints	0.47	liters	l
qt	quarts	0.95	liters	l
gal	gallons	3.8	liters	l
ft³	cubic feet	0.03	cubic meters	m³
yd³	cubic yards	0.76	cubic meters	m³
	TEMPERATURE (EXACT)			
°F	Fahrenheit temperature	5/9 (after subtracting 32)	Celsius temperature	°C

*1 in = 2.54 (exactly). For other exact conversions and more detailed tables, see NBS Misc. Publ. 286. Units of Weights and Measures. Price $2.25. SD Catalog No. C13.10.286.

Approximate Conversions from Metric Measures

Symbol	When You Know	Multiply By	To Find	Symbol
	LENGTH			
mm	millimeters	0.04	inches	in
cm	centimeters	0.4	inches	in
m	meters	3.3	feet	ft
m	meters	1.1	yards	yd
km	kilometers	0.6	miles	mi
	AREA			
cm²	square centimeters	0.16	square inches	in²
m²	square meters	1.2	square yards	yd²
km²	square kilometers	0.4	square miles	mi²
ha	hectares (10,000 m²)	2.5	acres	
	MASS (WEIGHT)			
g	grams	0.035	ounces	oz
kg	kilograms	2.2	pounds	lb
t	tonnes (1000 kg)	1.1	short tons	
	VOLUME			
ml	milliliters	0.03	fluid ounces	fl oz
l	liters	0.125	cups	c
l	liters	2.1	pints	pt
l	liters	1.06	quarts	qt
l	liters	0.26	gallons	gal
m³	cubic meters	35	cubic feet	ft³
m³	cubic meters	1.3	cubic yards	yd³
	TEMPERATURE (EXACT)			
°C	Celsius temperature	9/5 (then add 32)	Fahrenheit temperature	°F

°F -40°F   0   32   98.6   120 160 200   212°F
°C -40°C -20   0   20 37 40   60   80   100°C

SUMMARY

Two mathematical models that simulate sea ice motions from given
wind and current inputs are described. These models are evaluated as
candidates for predicting and simulating oil spill trajectories in ice-
covered waters. Simulated displacements of ice are compared with observed
displacements to evaluate the performance of these models during the
AIDJEX main field experiment in 1975-76. During this year-long experi-
ment, accurate winds and currents were available as input to the ice
motion models and a set of data buoys and camps provided motion observa-
tions for evaluating model performance. In addition to this performance
validation, requirements for computer resources, manpower and input data
are also presented.

A free-drift ice motion model is studied as the simplest possible
model for simulating daily ice motions. In this model, forces due to
winds, currents, Coriolis acceleration and sea surface tilt are balanced.
The daily ice motion at any selected site is obtained from the local
wind and current during that day. During the summer of 1975, say May
through September, simulated daily ice motions are compared with observed
motions. The mean displacement error is 0.010 m/s and the standard
deviation is 0.030 m/s. These errors may be attributed to uncertainty
in winds and currents. During the winter of 1975-76 when ice stress is
important, these errors increase. Then, a mean displacement error of
0.030 m/s and standard deviation of 0.107 m/s are apparent. Errors
increase roughly linearly during the fall, say October through December,
and decrease rapidly during April and May (of 1975, the previous year).

A complete ice dynamics model that describes internal ice stress
according to an elastic plastic material description is also studied.
This complete model is used to simulate ice motions at three selected
times during the study period in 1975-76. During summertime and early
fall the complete ice dynamics model is slightly more accurate than the
free-drift model, with mean displacement errors being 0.005 m/s and
standard deviation being 0.020 m/s. Although slightly better, these

errors are comparable with those of free drift. However, dramatic differences in the size of errors appear in late winter (January and February 1976). During this time the complete ice dynamics model gives mean displacement errors of 0.005 m/s and a standard deviation of 0.036 m/s. From this evidence we are able to conclude that the complete ice dynamics model is capable of describing ice motions to within the same accuracy throughout the year.

Both mathematical models of sea ice dynamics require winds and currents to determine the ice motions. The complete ice model also requires ice conditions and far-field boundary motion information. The free-drift computer requirements are minimal, while the complete model requires a computer with roughly 100K octal words of central memory. However, the input of wind and current fields for both models probably requires this size of computing facilities and graphic output of the results also dictates that a substantial computer be used. It is at present felt that manpower requirements for operational forecasting are similar for both models.

Both the free-drift and complete ice dynamics models are useful tools for U.S. Coast Guard requirements of predicting motions of oiled ice in the Beaufort Sea. During wintertime the complete model must be used if maximum accuracy is to be obtained, but during summertime the free-drift model appears to be nearly as accurate as the complete model.

TABLE OF CONTENTS

TABLE OF CONTENTS (Cont.)

LIST OF FIGURES

LIST OF FIGURES (Cont.)

LIST OF TABLES

Chapter 1
INTRODUCTION

1.1 OBJECTIVE

Recent lease sales (December 1979) of offshore tracts in the Beaufort Sea portion of the Arctic Ocean represent the beginnings of the development of oil fields in this marine environment. Exploratory drilling operations in both the U.S. and Canada must be expected to increase and be followed by production operations as the oil fields are developed. The thick sea ice cover on the Arctic Ocean is a formidable factor in these operations. Mobile pack ice is present year-round in the central Arctic. It is composed of many thick, multiyear ice floes that are typically a few kilometers in size and are separated by thin ice more recently grown on leads formed as the floes fracture and divide. The large-scale average thickness of the pack ice is roughly 3 m. As an opposite extreme, during the summer when air temperatures rise above freezing, melting and offshore winds combine to form an approximately 300-km-wide swath of open water along the Alaskan North Slope and the Mackenzie Delta. Thus, summertime drilling could take place (U.S. regulations do not allow summertime drilling in the Prudhoe Bay lease area, but it is the only time drilling is allowed in the Mackenzie Bay area of Canada) using techniques developed for shallow, midlatitude waters. After freeze-up, the coastal or continental region is ice covered except for leads and polynyas generated by ice deformations. The ice nearest shore is typically motionless because it is often grounded, is protected by shoreline irregularities and is strong enough to resist deformation by winds and currents. Between the mobile pack ice and the land-fast ice is the highly deformed stamukhi zone, an area in which shear and pressure ridges are found nearly everywhere.

This quick sketch of the ice conditions that appear in Arctic waters is included here to help indicate the range of applicability of the models presented in this report. Variations in the location and

1

extent of each ice zone are significant from year to year and during the course of each year. The large-scale ice drift models are intended to describe the behavior of pack ice, not the smaller-scale fast ice. Thus, some care must be exercised to ensure that the models are applied only under conditions which adequately simulate the appropriate physical processes.

This study is part of a U.S. Coast Guard program designed to provide methods to predict the movement of oil spills in Arctic and sub-Arctic coastal waters. These motion predictions are necessary to allow oil spill cleanup strategies to be selected and plans to be developed for handling individual oil spills. Defining the kinds of spills that can occur is not part of this study, but it is useful to note that an oil spill could range from a small release of fixed volume to an oil well blowout that continues unchecked for an entire year. Thus, a method is needed for tracking oil spills over periods ranging from a few days to many months.

A great amount of research has been performed to determine the fate and behavior of oil spilled in and under a sea ice cover. A synthesis of these results has been prepared as part of the Outer Continental Shelf Environmental Assessment Program[+] (Thomas, 1980). The most important result of that work is that oil will be transported primarily by the large-scale motions of the pack ice. Therefore, tracking of an oil spill becomes a problem of tracking the ice cover itself. The work presented in this study is focused on evaluating the performance of models that simulate pack ice motions to determine probable ice trajectories.

1.2 APPROACH

Two different mathematical models of sea ice dynamics are evaluated to learn how well each simulates observed motions under a full range of

[+] The Outer Continental Shelf Environmental Assessment Program (OCSEAP) is funded by the Bureau of Land Management through interagency agreement with the National Oceanic and Atmospheric Administration to respond to the needs of petroleum development off the Alaskan Continental Shelf.

ice conditions. The first is a free-drift model in which air and water drag, Coriolis force and sea surface tilt are the forces acting on the ice. This model neglects the ice stress that arises as a larger-scale effect of forces transmitted between individual ice floes. It is the simplest deterministic formulation that can be derived based on the driving forces applied by the atmosphere and the ocean. The second is a complete ice dynamics model that describes the internal ice stress as a hardening/softening, elastic-plastic material in which strength is a function of the instantaneous ice thickness distribution. This model, developed during AIDJEX[+], is the most sophisticated mathematical representation of the physical processes that control sea ice dynamics behavior that has been developed. The major features of the AIDJEX model are presented by Pritchard (1980); they are modified extensively and reformulated in his later work (Pritchard, 1981).

The performance of each model is evaluated by determining the difference between observed and simulated daily displacements (average velocities during a day) using data from AIDJEX buoys and manned camps. Several time periods during the 1975-76 AIDJEX main experiment are selected: 13-28 April 1975, 17-25 May 1975 and 27 January through 12 February 1976. These are the only periods for which AIDJEX model simulations are available. In addition, free-drift simulations are evaluated from June through December 1975. The scope of the work presented in this report is limited to evaluating the performance and estimating the resources required to use each model for oil spill tracking. However, our primary focus in this report is to evaluate the free-drift model and to learn how well it performs in comparison to the more complicated model.

The free-drift model is described completely. In this discussion, all forces acting on the ice (except internal ice stress) are presented. The planetary boundary layer model and oceanic mixed layer models show

---

[+]The Arctic Ice Dynamics Joint Experiment (AIDJEX), 1970-77, was a multi-nationally coordinated theoretical and field program aimed at gaining a better fundamental understanding of the physical behavior of sea ice.

how traction is transmitted from winds and currents. The minimum time
resolution of 1 day is identified and the ice response is explained.
The complete ice dynamics model, which is a reformulation of the early
AIDJEX model, is also presented in detail. The input data and the
computing resources required to use each model are listed.

Chapter 2

FREE-DRIFT MODEL

2.1 GENERAL DESCRIPTION

In 1979 the Outer Continental Shelf Environmental Assessment Program
(OCSEAP) funded a study by Flow Research Company of ice motions in the
Beaufort and Chukchi Seas (Thomas and Pritchard, 1979). The free-drift
model as taken from that report is described in this section. The
effect of model parameters on free-drift is studied by nondimensionalizing
the force balance equations driving the model.

An important consideration in applying the free-drift model is time
scale. Inertial effects are ignored in free-drift so that the model has
a resolution of 1 day. This is short enough to account for synoptic
variations in weather systems while still being long enough to average
out high frequency motions. If an ice trajectory for a month is desired,
it is tempting to apply the wind stress averaged over a month and make a
single calculation. This is not acceptable because nonlinearities in
the model require daily calculations of drift.

If a free-drift model is to be implemented, it is important to know
the quality of the data required to drive it. Free-drift calculations
require both air and water stress data for daily intervals to be input.
Both of these parameters are difficult to estimate accurately. Estimates
of the air stress require knowledge of the wind field, which is generally
calculated from the distribution of atmospheric pressure. In the Arctic
Ocean, this distribution is not well known. The water stress is due to
the relative motion of the ice with respect to the water. Estimates of
water stress thus require knowledge of geostrophic currents. These
currents vary from 0.01 to 0.03 m/s in the central Beaufort and are not
well known even for 1975 when many measurements were made. In practice,
and for all the free-drift calculations presented here, it is necessary
to assume a zero geostrophic current and accept this as a major source
of error.

2.2 FREE-DRIFT EQUATIONS OF MOTION

During free-drift, motion of the ice cover may be determined by considering momentum balance locally. The forces acting on the ice are air stress τ_a , water stress τ_w , Coriolis force $-mf \, k \times v$ and sea surface tilt $-mg\nabla H$. Momentum changes then occur as

$$m\dot{v} = \tau_a + \tau_w - mf \, k \times v - mg\nabla H \qquad (2.1)$$

where

m	is mass per unit area of ice,
v	is velocity in the horizontal plane,
$\dot{v}$	is material time rate of change of v,
τ_a	is traction exerted by the atmosphere on the upper surface of ice,
τ_w	is traction exerted by the ocean on the lower surface of ice,
f	is the Coriolis parameter,
k	is the unit vector in the vertical direction,
g	is acceleration due to gravity, and
H	is the height of the sea surface.

The air stress is determined from the geostrophic wind in the atmosphere as

$$\tau_a = \rho_a c_a \, |U| \, B_a U \qquad (2.2)$$

where

$$B_a = \begin{pmatrix} \cos \alpha & -\sin \alpha \\ \sin \alpha & \cos \alpha \end{pmatrix} \qquad (2.3)$$

and ρ_a is air density and c_a is the drag coefficient. The air stress is turned at an angle α to the applied geostrophic wind U . We have neglected the ice drift since it is two orders of magnitude smaller than the geostrophic wind. The geostrophic wind is determined from the surface barometric pressure field P as

$$U = -\frac{1}{\rho_a f} \, k \times \nabla P \, . \qquad (2.4)$$

The water stress satisfies a quadratic drag law similar to the atmosphere:

$$\underset{\sim}{\tau}_w = \rho_w c_w \left| \underset{\sim}{v} - \underset{\sim}{v}_g \right| \underset{\sim}{B}(\underset{\sim}{v} - \underset{\sim}{v}_g) \qquad (2.5)$$

where ρ_w is water density, c_w is the drag coefficient, $\underset{\sim}{v}_g$ is the ocean geostrophic current and

$$\underset{\sim}{B} = \begin{pmatrix} \cos{(\beta + \pi)} & -\sin{(\beta + \pi)} \\ \sin{(\beta + \pi)} & \cos{(\beta + \pi)} \end{pmatrix} , \qquad (2.6)$$

where β is the angle at which traction is applied by the current. The sea surface tilt defines the ocean geostrophic current in the form

$$mg\nabla H = - mf \underset{\sim}{k} \times \underset{\sim}{v}_g . \qquad (2.7)$$

The ice velocity may be determined at each point as a function of time whenever the barometric pressure field history is prescribed. Many authors have used the free drift relationships to analyze ice motions. Recently, McPhee (1980) has used this model to simulate motion and deformation of the AIDJEX manned array during the summer of 1975.

The results sought have a time resolution on the order of 1 day. For this case, inertia is negligible. Therefore, the analysis is performed for steady-state conditions. When shorter time-scale results are desired, the ice inertia may be included; but in this case the inertia of the water column is also significant (McPhee, 1978). Thus, the inertial contribution is not completely formulated. For both reasons we choose to neglect inertia completely and use the steady-state equations to calculate daily average velocities. In this case, Equation (2.1) becomes

$$\underset{\sim}{\tau}_a + \underset{\sim}{\tau}_w - mf \underset{\sim}{k} \times \underset{\sim}{v} - mg\nabla H = \underset{\sim}{0} . \qquad (2.8)$$

If the water stress (2.5) and sea surface tilt terms (2.7) are substituted into Equation (2.8), then

7

$$\underset{\sim}{\tau}_a + \rho_w c_w \left| \underset{\sim}{v} - \underset{\sim}{v}_g \right| \underset{\sim}{B} (\underset{\sim}{v} - \underset{\sim}{v}_g) - mf \, \underset{\sim}{k} \times (\underset{\sim}{v} - \underset{\sim}{v}_g) = \underset{\sim}{0} \ . \qquad (2.9)$$

But this force balance relates air stress $\underset{\sim}{\tau}_a$, geostrophic ocean currents $\underset{\sim}{v}_g$ and ice drift in a special way, namely, the ice velocity and current always appear as the difference $\underset{\sim}{v} - \underset{\sim}{v}_g$. Thus, if we introduce

$$\underset{\sim}{G} = \underset{\sim}{v} - \underset{\sim}{v}_g \ , \qquad (2.10)$$

then force balance becomes

$$\underset{\sim}{\tau}_a + \rho_w c_w \left| \underset{\sim}{G} \right| \underset{\sim}{B} \underset{\sim}{G} - mf \, \underset{\sim}{k} \times \underset{\sim}{G} = \underset{\sim}{0} \ . \qquad (2.11)$$

This equation may be rewritten in terms of water stress if desired as

$$\underset{\sim}{\tau}_a + \underset{\sim}{\tau}_w - mf \, \underset{\sim}{k} \times \underset{\sim}{G} = \underset{\sim}{0} \qquad (2.12)$$

where

$$\underset{\sim}{\tau}_w = \rho_w c_w \left| \underset{\sim}{G} \right| \underset{\sim}{B} \underset{\sim}{G} \ .$$

As a result of introducing $\underset{\sim}{G}$, the ice velocity relative to deep ocean currents, it is seen that it is this quantity that air stress affects. Therefore, contributions to ice drift due to air stress and to ocean current may be calculated separately. The air stress effect is found from Equation (2.11) and the ocean current is added directly in the form

$$\underset{\sim}{v} = \underset{\sim}{G} + \underset{\sim}{v}_g \ . \qquad (2.13)$$

2.3 MODEL RESPONSE

In order to understand model response, nondimensional variables are introduced that show explicitly how all material constants affect solutions and simplify the presentation and understanding of the results. The nondimensional variables have been determined by Pritchard and Thomas (1980) for the AIDJEX ice model.

We introduce nondimensional variables for velocity,

$$\overline{\underset{\sim}{v}} = \frac{\rho_w c_w}{mf} \underset{\sim}{v}$$

$$\overline{\underset{\sim}{U}} = \frac{\rho_w c_w}{mf} \underset{\sim}{U} \tag{2.14}$$

$$\overline{\underset{\sim}{G}} = \frac{\rho_w c_w}{mf} \underset{\sim}{G} \quad,$$

and for air and water stress,

$$\overline{\underset{\sim}{\tau}} = \frac{\rho_w c_w}{(mf)^2} \underset{\sim}{\tau} \quad, \tag{2.15}$$

and for pressure and position we introduce arbitrary scaling,

$$\overline{P} = P/P_R \tag{2.16}$$

$$\overline{\underset{\sim}{x}} = \underset{\sim}{x}/x_R \quad.$$

We introduce the nondimensional numbers

$$N_p = \frac{\rho_w c_w P_R}{\rho_a mf^2 x_R} \tag{2.17}$$

$$N_a = \frac{\rho_a c_a}{\rho_w c_w}$$

and the steady state equation of motion (2.11) then becomes

$$\overline{\underset{\sim}{\tau}}_a + |\overline{\underset{\sim}{G}}| \underset{\sim}{B}\overline{\underset{\sim}{G}} - \underset{\sim}{k} x \overline{\underset{\sim}{G}} = \underset{\sim}{0} \tag{2.18}$$

where air stress satisfies

$$\overline{\underset{\sim}{\tau}}_a = N_a |\overline{\underset{\sim}{U}}| \underset{\sim}{B}_a \overline{\underset{\sim}{U}} \quad. \tag{2.19}$$

The geostrophic wind is

$$\overline{\underset{\sim}{U}} = -N_p \underset{\sim}{k} x \overline{\nabla} \, \overline{P} \quad. \tag{2.20}$$

9

The relationship between ice velocity and applied air stress has
been described in a convenient form by Pritchard, Coon and McPhee (1977).
If we modify that work by using the present nondimensional variables,
then

$$\bar{\tau}_a = s Q \bar{G} \tag{2.21}$$

where

$$s = \left(|\bar{G}|^2 + 2 \, |\bar{G}| \, \sin \beta + 1 \right)^{\frac{1}{2}} \tag{2.22}$$

$$Q = \begin{pmatrix} \cos \delta & -\sin \delta \\ \sin \delta & \cos \delta \end{pmatrix}$$

where

$$\tan \delta = \tan \beta + \frac{1}{|\bar{G}| \cos \beta} \, . \tag{2.23}$$

The ice drift relative to geostrophic ocean currents is to the right of
the air stress by the angle δ. The forces acting on the ice are shown
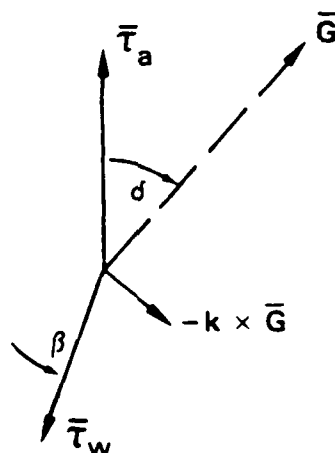in Figure 2.1. The ice drift appears as a dashed arrow.

Figure 2.1.   Free-Drift Force Balance and Ice Velocity

The magnitude of air stress and ice drift are related by

$$|\overline{\underset{\sim}{\tau}}_a| = s \, |\overline{\underset{\sim}{G}}| \quad , \tag{2.24}$$

which is displayed in Figure 2.2. We have chosen to invert Equation (2.24) for graphical representation since we anticipate $\overline{\underset{\sim}{\tau}}_a$ to be given as input and ice drift calculated as output. The angle δ also varies with air stress magnitude as may be seen by solving Equations (2.23) and (2.24) simultaneously. In Figure 2.3 we present the results. It is seen that the turning angle depends significantly on the oceanic boundary layer Ekman angle β . This is not true of ice speed which is insensitive to changes in β .

The ice speed is a nonlinear function of air stress magnitude, and the turning angle depends on air stress magnitude, too. Thus, the response is nonlinear and therefore the model cannot be used directly on monthly mean air stress.

To circumvent this problem, we look at the relationship between air stress magnitude and ice drift speed which is nearly parabolic. By introducing the quadratic atmospheric boundary layer model, we seek a linear relationship between geostrophic wind and ice drift. We find

$$N_a \, |\overline{\underset{\sim}{U}}| \, \underset{\sim}{B}_a \overline{\underset{\sim}{U}} = s\underset{\sim}{Q}\overline{\underset{\sim}{G}} \quad . \tag{2.25}$$

The wind and ice speed are related by

$$N_a \, |\overline{\underset{\sim}{U}}|^2 = s \, |\overline{\underset{\sim}{G}}| \quad . \tag{2.26}$$

This relationship is presented in Figure 2.4. It is seen that the ice speed is nearly a linear function of the wind speed. This observation was noted by both M. G. McPhee (1980) and A. S. Thorndike (personal communications) and led them to prefer using geostrophic wind rather than air stress in their free-drift analyses.
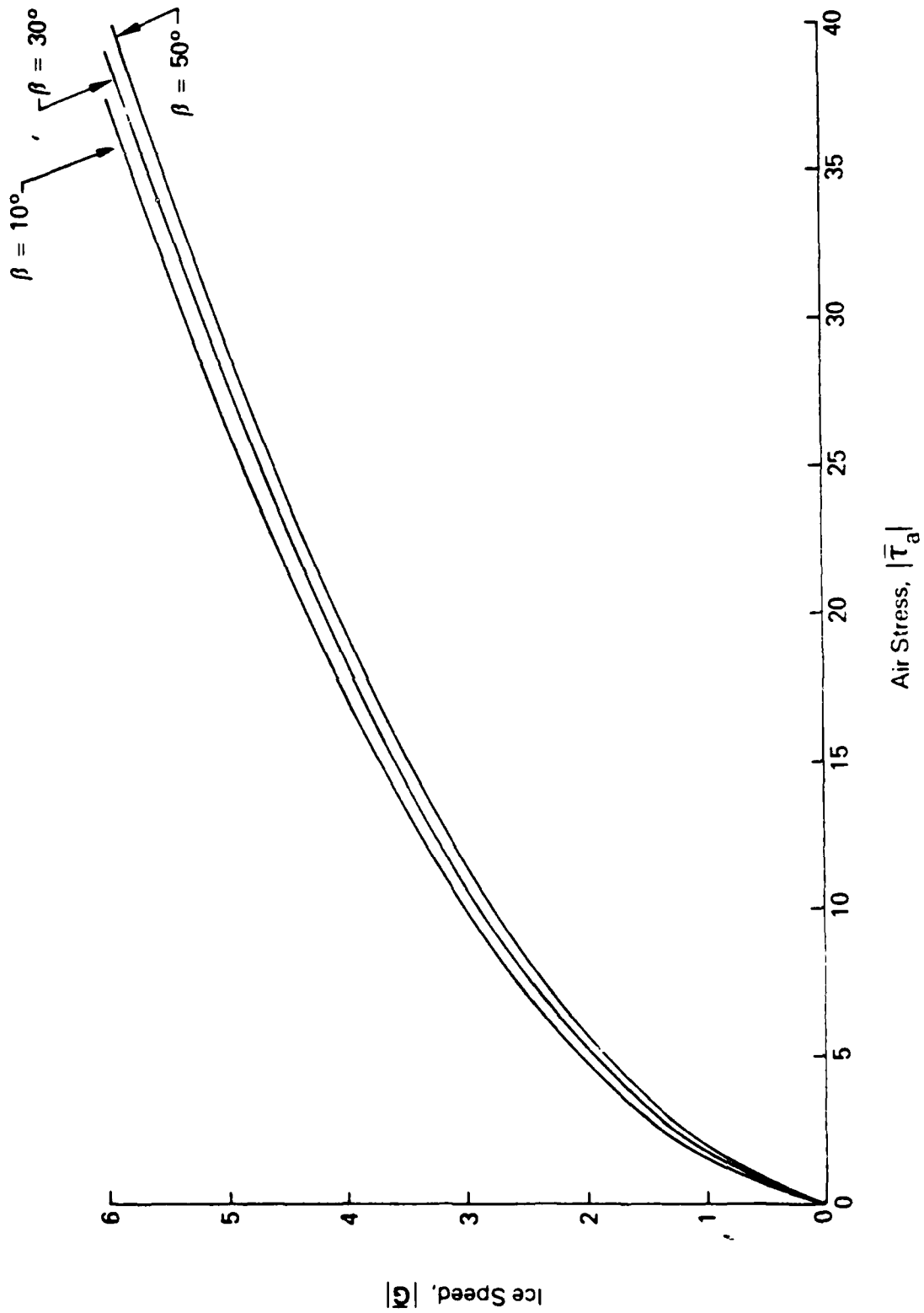
Figure 2.2. Relationship Between Nondimensional Relative Ice Speed $|\overline{G}|$ and Nondimensional Air Stress Magnitude $|\overline{\tau}_a|$ for a Range of Oceanic Boundary Layer Turning Angles β

Figure 2.3. Relative Ice Velocity Orientation δ as a Function of Nondimensional Air Stress Magnitude $|\bar{\tau}_a|$ for a Range of Oceanic Boundary Layer Turning Angles β
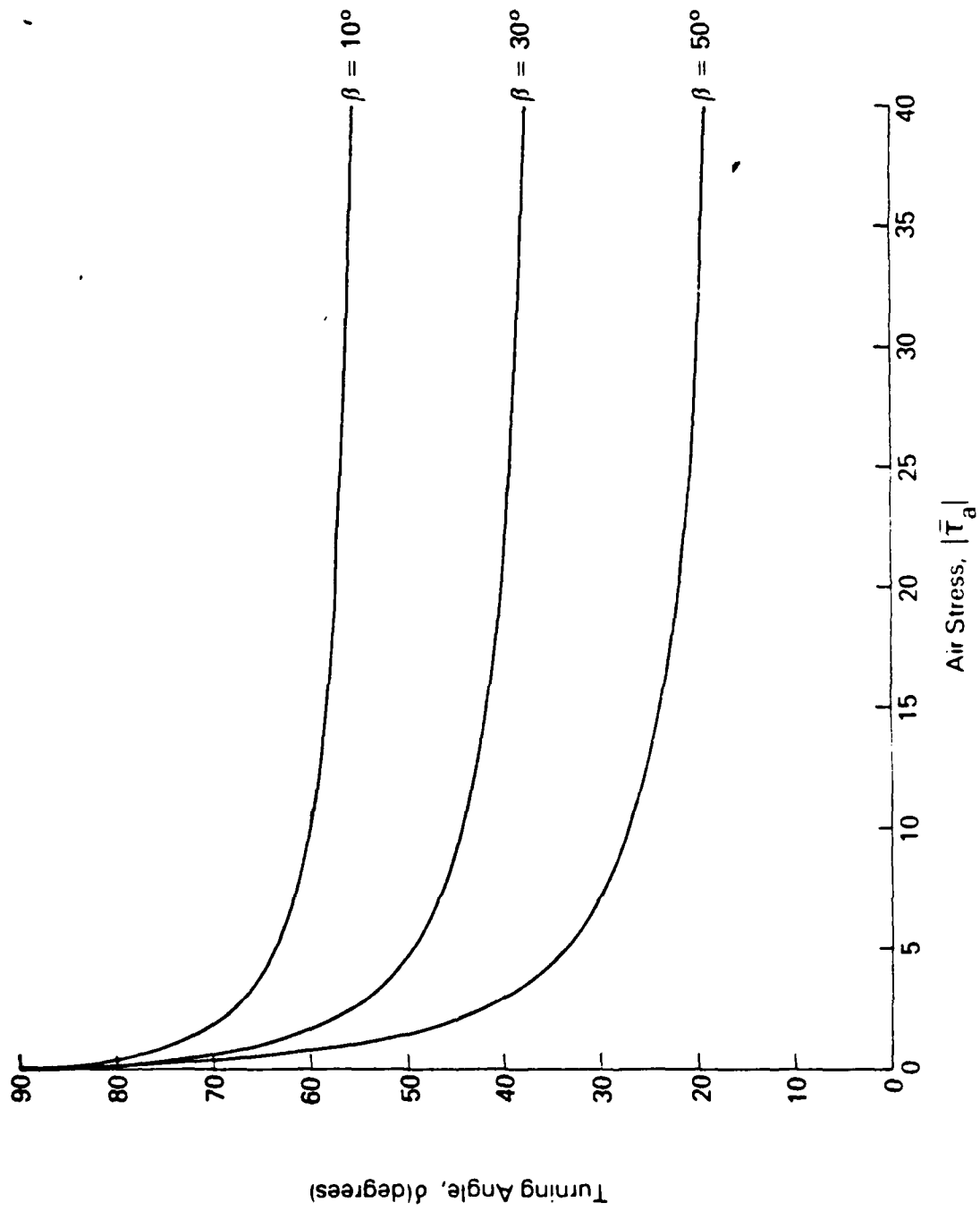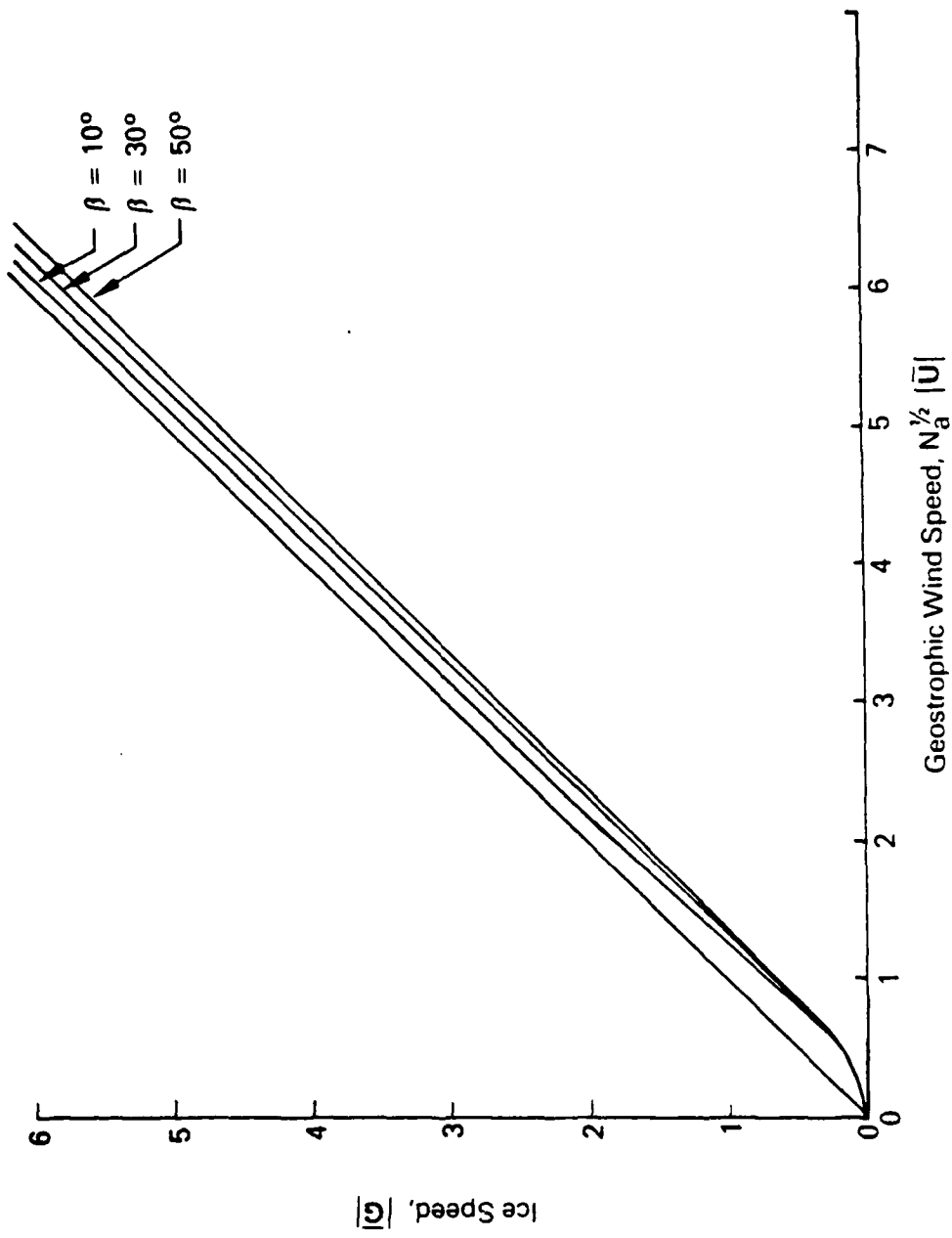
13

Figure 2.4. Relationship Between Nondimensional Relative Ice Speed $|\bar{G}|$ and Nondimensional Geostrophic Wind Speed $N_a^{1/2}|\bar{U}|$ for a Range of Oceanic Boundary Layer Turning Angles β

14

The angle between geostrophic wind and ice drift is controlled by $B_{\sim a}^T Q$, where the superscript T represents the transpose of the matrix $B_{\sim a}$ and since

$$N_a \, |\overline{U}| \; \overline{U} = sB_{\sim a}^T \underset{\sim}{Q}\overline{G} \quad , \tag{2.27}$$

we see that the ice drift is oriented at an angle $\delta - \alpha$ to the right of the geostrophic wind. This relationship is shown in Figure 2.5. It is seen that the turning angle depends strongly on wind speed. Therefore, the relationship is not linear and the monthly average geostrophic wind cannot be used directly to obtain the monthly ice motion. In practice, however, it is possible that a constant angle (say $\delta = 45^\circ$) would provide a useful approximation to longer-term drift.

Due to the nonlinearity in these relationships, the decision was made to process historical winds on a daily basis and sum up the daily ice displacements to obtain monthly values. The nondimensional formulation has simplified the task of determining the effect of material parameters, however. To estimate these effects better, consider the relationship between ice speed and geostrophic wind. The ice speed is nearly a linear function of geostrophic wind speed at higher values. If Equation (2.26) is rewritten as

$$y^2 = (x^2 + ax + 1)^{\frac{1}{2}} x \quad , \tag{2.28}$$

where

$$y = N_a^{\frac{1}{2}} |\overline{U}| \;\; , \;\; x = |\overline{G}| \;\; \text{and} \;\; a = 2 \sin \beta$$

are introduced for notational convenience, then an expansion may be made for large values of x :
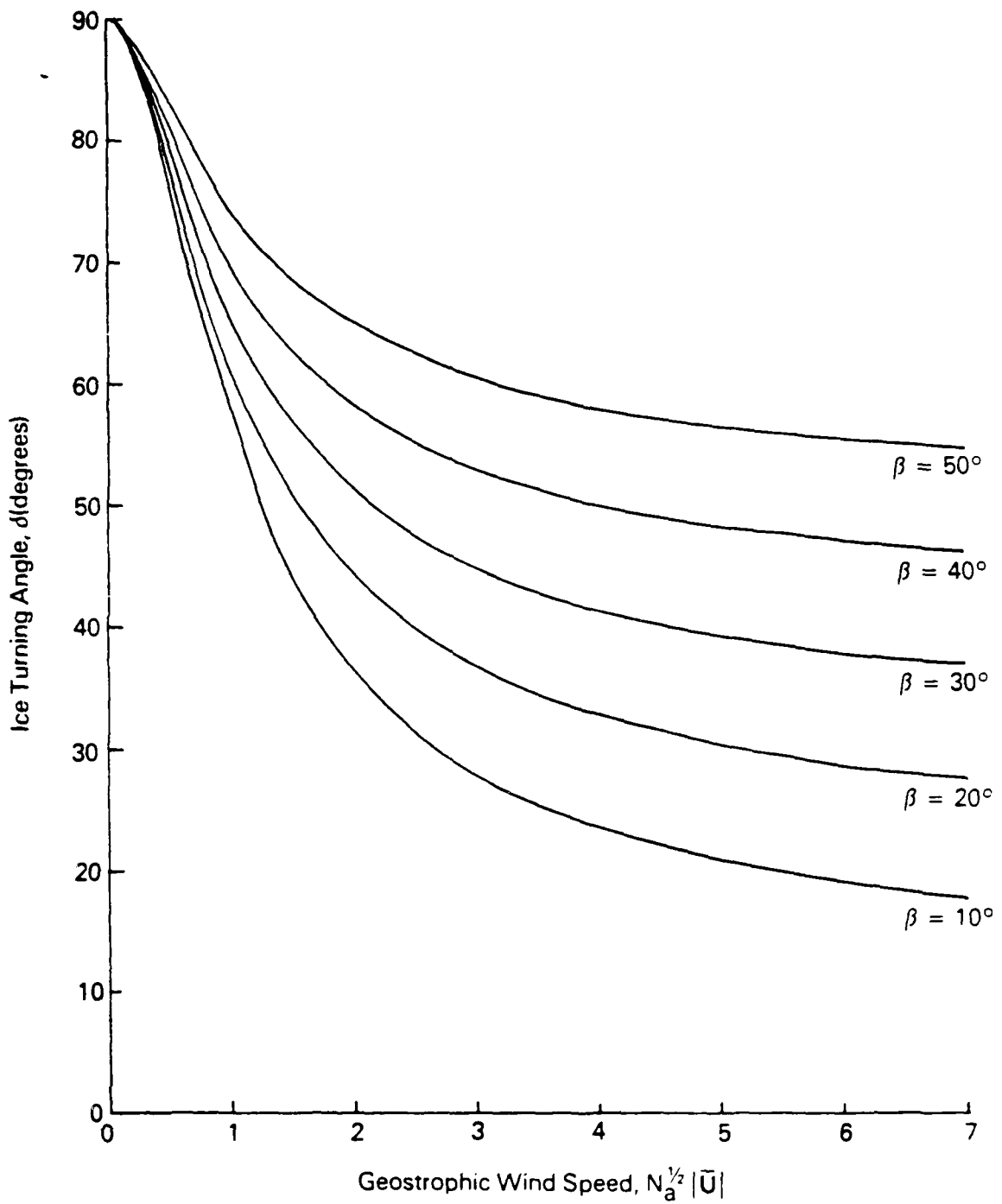
$$y = (1 + ax^{-1} + x^{-2})^{\frac{1}{2}} x$$

Figure 2.5. Relative Ice Velocity Orientation δ as a Function of Nondimensional Geostrophic Wind Speed $N_a^{1/2}|\bar{U}|$ for a Range of Oceanic Boundary Layer Turning Angles β

16

and then

$$y = (1 + \frac{1}{4} ax^{-1} + \ldots)x \quad .$$

Finally,

$$y = \frac{a}{4} + x + 0(x^{-1}) \quad . \tag{2.29}$$

Returning to the original notation and inverting results in

$$|\overline{G}| \cong N_a^{\frac{1}{2}} |\overline{U}| - \frac{1}{2} \sin \beta \quad , \tag{2.30}$$

which provides the coefficients of the linear relationship. If the nondimensional solutions given by Equations (2.23) and (2.30) are re-written in terms of physical variables, then

$$|\underset{\sim}{G}| \cong N_a^{\frac{1}{2}} |\underset{\sim}{U}| - \frac{mf}{2\rho_w c_w} \sin \beta \tag{2.31}$$

and

$$\tan \delta = \tan \beta + \frac{mf}{\rho_w c_w |\underset{\sim}{G}| \cos \beta} \quad . \tag{2.32}$$

It is seen that the ice speed is insensitive to changes in mass m because it occurs only in the constant term, which is small. But the ratio of drag coefficients in the atmosphere and ocean, N_a , affects ice speed as a square root function. Therefore, all parameters have a modest affect on ice speed. However, in the range of parameters anticipated, all can cause large changes in the turning angle. For example, increasing β from 20° to 30° increases the turning angle by about 10°. This is comparable to increasing the water drag or decreasing the mass density m by about 10 percent at higher speeds. The changes are smaller when winds are lower. The ratio of drag coefficients, N_a , affects the turning angle indirectly through the ice speed. If a 10 percent increase in N_a causes a 5 percent increase in $|\underset{\sim}{G}|$, this in turn will cause about a 5° decrease in the turning angle.

17

Some consideration must be given to the special conditions that exist near the edge of the pack ice during summer when there is appreciable open water. In this case, the ice concentration is often low. The model has not been tested thoroughly under these conditions; however, the following argument should eliminate serious concern. In the free-drift model (Equation 2.11), the areal mass density is scaled down in proportion to the ice concentration. Similarly, the traction exerted by the atmosphere and the ocean on the ice in Equations (2.2) and (2.11) should be proportional to the relative area covered by ice - but this is just the concentration. Therefore, each term in the free-drift momentum balance is changed by the same amount, and the relationship between ice motion and geostrophic wind is unchanged.

2.4 PARAMETERS

The main driving force of the free-drift model is the air stress. The air stress is computed from the geostrophic wind field as

$$\underset{\sim}{\tau}_a = \rho_a c_a \left| \underset{\sim}{U} \right| \underset{\sim}{B}_a \underset{\sim}{U} \tag{2.2 bis}$$

$$\underset{\sim}{B}_a = \begin{pmatrix} \cos \alpha & -\sin \alpha \\ \sin \alpha & \cos \alpha \end{pmatrix} \tag{2.3 bis}$$

where c_a is a drag coefficient, ρ_a is the air density, $\underset{\sim}{U}$ is the geostrophic wind and α is the angle of the air stress from the geostrophic wind. The geostrophic winds are computed from the surface pressure field as

$$\underset{\sim}{U} = - \frac{1}{\rho_a f} \, k \times \nabla P \tag{2.4 bis}$$

where f is the Coriolis parameter.

Leavitt et al. (1978a,b) have estimated c_{10} , the 10-m drag coefficient, to be 0.0025 using AIDJEX data. They believe c_{10} to be accurate to ± 20 percent. Albright (1980) has computed the ratio U_{10}/U to-be 0.55 in the summer, using the AIDJEX data set. Computing the drag coefficient as

$$c_a = \left(\frac{U_{10}}{U}\right)^2 c_{10} \tag{2.33}$$

and using the above values of U_{10}/U and c_{10} gives $c_a = 0.0008$ for the summer. Albright (1980) also gives the summer value of $\alpha = 24^o$ with a standard deviation of 5°.

The air density, ρ_a , is computed as the monthly average of all the densities computed from AIDJEX temperature data. The "within month" standard deviation of ρ_a is about 2 percent while the range of variation from month to month is about 12 percent.

Reliable data on the mean thickness of the ice for 1975 are not available. We used the computed mean thickness presented in Thorndike et al. (1975), where an initial ice thickness distribution as measured by under-ice profile is followed through 2 years of known deformation and climatological thermodynamics. Table 2.1 gives the air density and ice thickness used in free-drift simulations. One check point of these data appears during April 1976 when an under-ice profile was obtained by upward-looking, submarine-mounted sonar. Analysis of these data by Wadhams and Horne (1978) shows a mean draft of 3.7 m (average of two tracks of 200 km length crossing under camp Caribou). Converting mean draft to mean ice thickness is accomplished by multiplying by the ratio of ocean-water density to ice density $\rho/\rho_i = 1.1$. The mean ice thickness during April 1976 is observed to be 4.1 m. This observed value is about 5 percent larger than the April values calculated by Thorndike et al. (1975). It is likely that values in Table 2.1 for January through April are somewhat low since mean thickness should increase throughout winter. The history shown is probably dependent on initial conditions and on the specific deformation history used by Thorndike et al. (1975). In any case, the values are reasonable and an uncertainty of 5 percent is acceptable.

Table 2.1. SEASONAL VARIATIONS IN ICE THICKNESS AND AIR DENSITY.

Month	$\bar{h}$ (m)	ρ_a (kg/m^3)
January	3.90	1.47
February	3.90	1.47
March	3.90	1.45
April	3.90	1.40
May	3.70	1.36
June	3.55	1.31
July	3.25	1.29
August	2.95	1.29
September	3.30	1.33
October	3.70	1.38
November	4.15	1.44
December	4.05	1.46

The Coriolis parameter is computed as

$$f = 2\Omega \sin \phi \tag{2.34}$$

where $\Omega = 7.29 \times 10^{-5}$ rad/s and ϕ = latitude.

The water stress is computed as

$$\underset{\sim}{\tau}_w = \rho_w c_w \left| \underset{\sim}{v} - \underset{\sim}{v}_g \right| \underset{\sim}{B}(\underset{\sim}{v} - \underset{\sim}{v}_g) \tag{2.5 bis}$$

$$\underset{\sim}{B} = \begin{pmatrix} \cos (\beta+\pi) & -\sin (\beta+\pi) \\ \sin (\beta+\pi) & \cos (\beta+\pi) \end{pmatrix} \tag{2.6 bis}$$

The water drag coefficient and turning angle used were $c_w = 0.0055$ and $\beta = 23^{\circ}$, as given in McPhee (1980). The geostrophic current $\underset{\sim}{v}_g$ was set to zero as previously explained.

Chapter 3
COMPLETE ICE DYNAMICS MODEL

3.1 GENERAL DESCRIPTION

The sea ice dynamics model describes the large-scale mechanical behavior of the thin ice cover floating on a polar ocean. Thus, we require a mathematical description of forces acting on a large-scale typical element of ice. The model is two-dimensional in the sense that all motions are constrained to lie in the surface of the ocean. But the thickness of pack ice is variable, being made up of thick old floes, open water and thin young ice growing on leads. The amounts of open water and thin ice have a dominant influence both on the rate of vertical heat transfer from the ocean to the atmosphere and on the strength or ability of the ice to resist wind or ocean current loads. The variations in thickness are characterized by a thickness distribution that describes the fraction of an elemental region covered by ice of each thickness. The mathematical equation describing changes in the ice thickness distribution represents mass balance. Ice thickness distribution is analogous to a set of equations governing changes in species concentrations in a mixture, except that the ice thickness distribution describes an infinite set of species differentiated only by their thicknesses. As in mixture theory, species interact thermally and by redistribution, but no relative motion is allowed between species.

The constitutive laws are introduced to relate stress in the ice pack to deformation. This stress is a resultant integrated through thickness much like the stress resultant in plate or shell theory. In addition, the formation and modification of leads and ridges as the ice cover deforms changes the ice thickness distribution. This creation of open water in leads and the formation of thick ridges from thin ice requires a constitutive law describing the production and conversion of ice due to mechanical redistribution.

All fundamental aspects of this mathematical model have been developed and described previously. These include balance of mass, momentum and mechanical energy. Therefore, we present the governing equations without justifying the assumptions made to obtain each balance law. The constitutive laws, however, are changed enough to require a more thorough explanation. But even with these changes, the type of behavior is unchanged. In the remainder of this section, each balance law and constitutive equation is presented.

3.2 MOMENTUM BALANCE

In the plane of motion of the sea ice, the momentum balance is expressed as

$$m\dot{\underset{\sim}{v}} = \underset{\sim a}{\tau} + \underset{\sim w}{\tau} - mf\ \underset{\sim}{k} \times \underset{\sim}{v} - mg\nabla H + \nabla \cdot \underset{\sim}{\sigma} \quad , \tag{3.1}$$

where

m is mass per unit area of ice,

$\underset{\sim}{v}$ is ice velocity in the horizontal plane,

$\dot{\underset{\sim}{v}}$ is material time rate of change of $\underset{\sim}{v}$,

$\underset{\sim a}{\tau}$ is traction exerted by the atmosphere on the upper surface of ice,

$\underset{\sim w}{\tau}$ is traction exerted by the ocean on the lower surface of ice,

f is the Coriolis parameter,

g is acceleration due to gravity,

H is the height of the sea surface,

$\underset{\sim}{k}$ is the unit vector in the vertical direction, and

$\underset{\sim}{\sigma}$ is the Cauchy stress resultant in excess of hydrostatic equilibrium (two-dimensional).

The horizontal position vector $\underset{\sim}{x}$ and the vertical unit vector $\underset{\sim}{k}$ are expressed in a right-handed Cartesian coordinate system. Velocity is the material rate of change of position, $\dot{\underset{\sim}{x}} = \underset{\sim}{v}$.

The acceleration term in the momentum balance is generally much smaller than the other terms due to the fact that the acceleration of the ice is generally small.

The air stress is a dominant driving force in the momentum balance. For a typical day, it is the largest single contribution to the horizontal force balance. Because air stress is variable from day to day, however, the slowly varying ocean current can often provide a larger contribution to long-term motions. The air stress τ_a is given as a quadratic function of the geostrophic velocity U (Brown, 1976):

$$\tau_a = \rho_a c_a |U| \; B_a U \quad , \tag{3.2}$$

where

$$B_a = \begin{pmatrix} \cos \alpha & -\sin \alpha \\ \sin \alpha & \cos \alpha \end{pmatrix} , \tag{3.3}$$

and $\rho_a = 1 \text{ kg/m}^3$ is air density and $c_a = 0.0008$ is the drag coefficient. The air stress is turned at an angle $\alpha = 28°$ counterclockwise from the applied geostrophic wind U (Albright, 1980; Leavitt, 1980).

The effect of the oceanic boundary layer on ice motion has also been modeled as a quadratic relation between the traction τ_w exerted on the lower surface of the ice and the ice velocity relative to the geostrophic currents v_g (McPhee, 1975). The traction is applied at an angle $\beta = 23°$ to the relative velocity:

$$\tau_w = \rho_w c_w |v - v_g| B(v - v_g) , \tag{3.4}$$

where

$$B = \begin{pmatrix} -\cos \beta & \sin \beta \\ -\sin \beta & -\cos \beta \end{pmatrix}, \tag{3.5}$$

and $\rho_w = 1000 \text{ kg/m}^3$ is water density and $c_w = 0.0055$ is the drag coefficient. Geostrophic currents are considered to be steady, so time variations do not appear.

The Coriolis force exerted on sea ice depends on the ice velocity, the Coriolis parameter and the mass of sea ice. Within the AIDJEX model, the mass of the sea ice is determined through the ice thickness distribution as the ice density $(\rho = 900 \text{ kg/m}^3)$ times the mean thickness.

The ocean tilt term in the momentum balance arises from a varying sea surface height which, by balancing the hydrostatic head, determines the geostrophic flow in the ocean:

$$m g \nabla H = -mf \; \underset{\sim}{k} \times \underset{\sim}{v}_g \quad . \qquad (3.6)$$

The last term of the momentum balance is the divergence of internal ice stress. The stress is more accurately called a Cauchy stress resultant in excess of hydrostatic equilibrium (Coon et al., 1974). The stress state is related to the deformation history by an elastic-plastic constitutive law that is described in Section 3.5.

3.3 MASS BALANCE

One objective of AIDJEX was to relate the observed morphology of the ice to its field of motion. A model of this relation has been framed in the theory of the ice thickness distribution. Here the ice pack is viewed as a mixture of many different thicknesses. A balance equation is written to describe how each thickness category changes in response to the deformation and the thermodynamic forcing. While this theory does not attempt to describe the orientation or spacing of leads or pressure ridges, it does account for their net effect by keeping track of the amounts of open water and of thick, pressure-ridged ice. Many of the large-scale properties of the ice pack, such as its mass, its strength and its ability to insulate the atmosphere from the ocean, depend on the thickness distribution. It can, therefore, be viewed as a fundamental state variable.

Balance of mass is the principle that provides an equation governing the thickness distribution. Following Coon et al. (1974) and Thorndike et al. (1975) we write

24

$$\dot{G} + f_g \frac{\partial G}{\partial h} = \Psi - G \nabla \cdot \underset{\sim}{v} \qquad\qquad (3.7)$$

where

G($\underset{\sim}{x}$, h, t)   is the fraction of area in the vicinity of point $\underset{\sim}{x}$ at the time t that is covered by ice thinner than the ice thickness h ,

f$_g$(h, t)   is the growth rate of ice and may be different for each thickness and time, and

Ψ is a redistribution function that describes mechanical conversion of ice between categories.

Changes in the relative area covered by ice in each category are controlled by both thermodynamic growth and ablation $(f_g \frac{\partial G}{\partial h})$ and by mechanical redistribution (Ψ) . The remaining term $(G \nabla \cdot \underset{\sim}{v})$ is needed to account for changes in area since G indicates a fraction of present, not initial, area. The time rate of change $\dot{G}$ is a material rate.

The fraction of open water in an area is described by the zero-thickness category of ice, G($\underset{\sim}{x}$, 0, t) ; so the ice compactness is easily found by subtracting this quantity from unity. It should be noted that in this model there is no oceanic heat storage; open water formed during an opening or shearing episode is immediately frozen into thin ice during the "freezing season" when f_g(0, t) is positive. For this reason and because it is difficult, if not impossible, to differentiate between open water and thin ice using available remote sensors, we normally do not try to separate open water from thin ice, say less than 0.10 m thick, in simulated results of ice behavior.

The rate of mechanical production of ice of all thicknesses h and thinner is Ψ(h) , where we suppress dependence on $\underset{\sim}{x}$ and t which enter implicitly through G . Ice is produced in this range of categories by the formation of leads and by conversion from other categories during ridging. This mechanical redistribution of ice between categories changes the relative fraction of area covered by ice of each thickness category as seen in Equation (3.7). The amount of ridging that occurs at a location depends on the history of the motion of that ice. The

25

thickness distribution serves as the critical measure of the result of that history of deformation. Therefore, we assume that the instantaneous thickness distribution is adequate to describe the history and that only the instantaneous rate of deformation has an influence on redistribution. Furthermore, we assume that processes that redistribute ice are nonrecoverable and thus are associated with permanent deformations.

3.4 MECHANICAL ENERGY BALANCE

· The rate at which work is done on an elemental region of pack ice by all forces acting on the ice is obtained by forming an inner product of the ice velocity with each force in the momentum balance (Coon and Pritchard, 1979; Pritchard et al., 1979; Thomas and Pritchard, 1980). As a result of this mathematical manipulation, a mechanical energy balance is found in the form

$$\dot{\kappa} + \dot{U}_e = P_a - P_o - P_g + P_f - P_\ell \quad , \tag{3.8}$$

where

$\kappa = 1/2 \; m\underset{\sim}{v}^T\underset{\sim}{v}$ is kinetic energy density (the superscript T indicates the transpose),

$U_e = \text{tr} \; \underset{\sim}{\sigma} \; \underset{\sim}{e}$ is recoverable strain energy density ($\underset{\sim}{e}$ is elastic strain),

$P_a = \underset{\sim}{v}^T\underset{\sim}{\tau}_a$ is power input to the ice from the atmosphere by surface traction,

$P_o = -\underset{\sim}{v}^T\underset{\sim}{\tau}_w$ is power loss from the ice to the ocean by surface traction from the oceanic mixed layer,

$P_g = mg \; \underset{\sim}{v}^T\nabla H$ is the rate of increase of gravitational potential energy due to ice movement up the sea surface slope,

$P_f = \nabla \cdot (\underset{\sim}{v}^T\underset{\sim}{\sigma})$ is divergence of the stress flux, the rate at which energy is transferred horizontally through the ice cover, and

$P_\ell = \text{tr} \; \underset{\sim}{\sigma} \; \underset{\sim}{D}_p$ is dissipative stress power, the rate at which energy is dissipated by the stress state $\underset{\sim}{\sigma}$ during permanent deformations $\underset{\sim}{D}_p$.

26

The mechanical energy balance relationship has proven to be an important interpretive tool. It serves to provide a measure of the level of activity due to storms and to understand better the energy budget of polar oceans. Energetic events are strongly amplified since P_a is proportional to the wind speed cubed when ice drift is a linear function of wind speed. Furthermore, the small-scale mechanisms of energy dissipation occurring during ridging, in the form of gravitational potential energy increases and frictional losses from sliding of ice blocks into ridges, have been estimated directly (Rothrock, 1975). An additional shear ridging energy sink is discussed later in this chapter. These dissipative mechanisms are related to the large-scale dissipative stress power to constrain the constitutive laws. Thus, if p is the rate of dissipation of energy from all subscale mechanisms, it must equal the dissipation rate of stress during deformation. Therefore,

$$P_\ell = p . \tag{3.9}$$

3.5 CONSTITUTIVE LAWS

The set of constitutive laws contains relationships describing stress and redistribution in terms of the deformation history. Both are intended to describe the large-scale average behavior of the ice cover over length scales on the order of tens of kilometers. This average behavior is made up of the formation of many randomly oriented cracks, leads and ridges, assuming enough features are present to allow a homogeneous, isotropic behavior. The material behavior is assumed to be rate independent, as determined from a detailed analysis of ridge formation (Parmerter and Coon, 1972; Coon, 1974). The material response is assumed to be plastic because of this rate independence and because of the fact that ridges appear to have limited heights when formed from an ice sheet of fixed thickness. The material model to be described has five separate elements that are required to specify completely the internal ice stress for a given deformation history. These elements, which have much in common with other elastic-plastic material models, are: yield surface, flow rule, elastic response, kinematic relationship

27

and hardening law. The first four of these elements are now discussed, while the fifth is introduced after describing the ice redistribution law on which it depends.
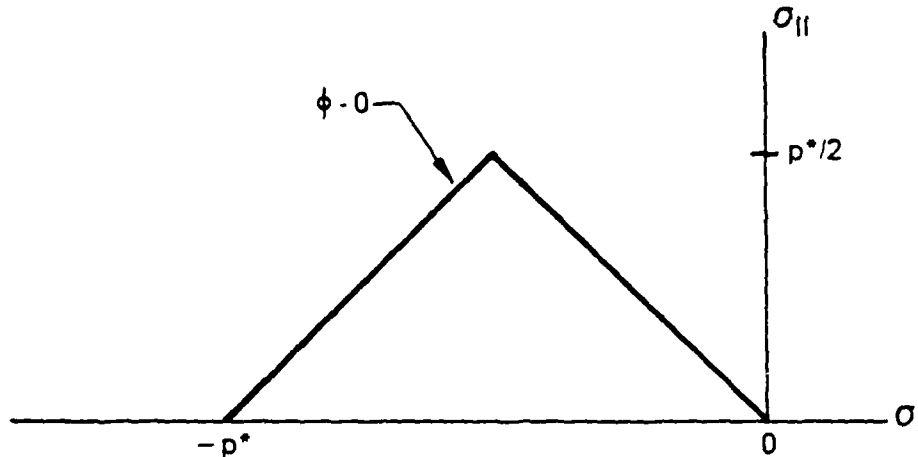

Figure 3.1. Diamond Yield Surface for Large-Scale Sea Ice Model

The stress state in any plastic model is constrained to lie within the yield surface. For an isotropic model, this function depends only on the stress invariants and not on the principal direction. Thus,

$$\phi(\sigma_I, \sigma_{II}, p^*) \le 0 \quad , \tag{3.10}$$

where $\sigma_I = 1/2 \text{ tr } \underset{\sim}{\sigma}$ (negative pressure), $\sigma_{II} = (1/2 \text{ tr } \underset{\sim}{\sigma}'\underset{\sim}{\sigma}')^{\frac{1}{2}}$ (maximum shear), $\underset{\sim}{\sigma}' = \underset{\sim}{\sigma} - \sigma_I \underset{\sim}{1}$ and p^* is the isotropic compressive strength. This strength will be shown to be a function of thickness distribution. The yield surface chosen for sea ice is shown in Figure 3.1. Along the straight-line portion of $\phi = 0$ passing through the origin, the stress state is that of uniaxial compression. Simulations of sea ice dynamics during January 1976 and of ice flow through the Bering Strait show that it is important to use this "tensile cutoff" line to define part of the yield surface (Pritchard, 1978; Reimer et al., 1979; Pritchard and Reimer, 1979). The other straight line used to complete the yield surface is chosen for simplicity. It reduces the shear strength by a

28

factor of 2 compared to the triangular yield surface which has the largest possible shear strength compatible with tensile cutoff, a concave surface and a compressive strength of p^*. Since the effective strength of the ice cover over length scales of tens of kilometers cannot be measured by direct, controlled experiments, we have estimated the values of p^* from simulations of complicated and uncontrolled large-scale ice behavior. A careful choice of wind, current and ice conditions has allowed simulations to be performed that show strengths in the range of 10^4 to 10^5 N/m for ice conditions common to the Beaufort Sea during the winter. It is worth noting that strengths below 10^4 N/m have little influence on ice motions, although we do not know the effect of ice stress on deformation at this strength level. This knowledge, sparse as it is, provides one test of the reasonableness of the strength values determined in the hardening/softening plastic model to be presented in the remainder of this section.

The next three elements of the plastic response are unchanged from previous forms of the model (Coon et al., 1974; Pritchard, 1975; Coon, 1980). When the stress state in the ice lies inside the yield surface, then the stress $\underset{\sim}{\sigma}$ is a function of the elastic strain $\underset{\sim}{e}$:

$$\underset{\sim}{\sigma} = (M_1 - M_2) \underset{\sim}{1} \, \mathrm{tr} \, \underset{\sim}{e} + 2M_2 \underset{\sim}{e} \quad , \tag{3.11}$$

where M_1 and M_2 are elastic moduli that may depend on the thickness distribution. The elastic moduli are normally chosen to be constant and large enough so that elastic response is a representation of rigid behavior. The elastic strain satisfies the kinematic relation

$$\underset{\sim}{\dot{e}} - \underset{\sim\sim}{We} + \underset{\sim\sim}{eW} = \underset{\sim}{D} - \underset{\sim}{D}_p \quad , \tag{3.12}$$

where $\underset{\sim}{D} = \frac{1}{2} (\underset{\sim}{L} + \underset{\sim}{L}^T)$ is stretching, $\underset{\sim}{W} = \frac{1}{2} (\underset{\sim}{L} - \underset{\sim}{L}^T)$ is spin and $\underset{\sim}{L} = \underset{\sim}{\nabla} \underset{\sim}{v}$ is the velocity gradient.

When the stress state is on the yield surface $\phi = 0$, plastic stretching occurs. During plastic flow, the stress is constrained to

the loading surface. The plastic stretching $D_{\sim p}$ satisfies the associated
flow rule

$$D_{\sim p} = \lambda \frac{\partial \varphi}{\partial \sigma_{\sim}} \text{, where } \lambda > 0 \quad , \tag{3.13}$$

which requires that plastic stretching be orthogonal to the loading
function at the instantaneous stress state.

The redistribution function Ψ retains the general form developed
by Thorndike et al. (1975). This constitutive law is expressed as a
function of permanent or plastic stretching $D_{\sim p}$ in the form

$$\Psi = D_p \left[\alpha_o(\theta) + \alpha_r(\theta) \, W_r \right] . \tag{3.14}$$

Invariants of the irreversible stretching tensor are the dilating
$D_I = \text{tr} \, D_{\sim p}$ and shearing $D_{II} = (2 \, \text{tr} \, D'_{\sim p} D'_{\sim p})^{\frac{1}{2}}$, where $D'_{\sim p} = D_{\sim p} - 1/2 \, D_I \underset{\sim}{1}$.
These invariants are equal to the sum and difference of the principal
stretching components, respectively. Another set of stretching invariants,
used by Nye (1976), is more valuable for describing stretching dependence
of the redistribution function. This set includes $D_p = (D_I^2 + D_{II}^2)^{\frac{1}{2}}$
and $\theta = \text{atan} \, (D_{II}/D_I)$, which are measures of the rate of stretching
D_p and the amount of shearing relative to dilating (θ) . The linear
dependence of Ψ on D_p ensures that the redistribution process is
rate independent, a property that is consistent with the elastic-plastic
stress constitutive law. The term $\alpha_o + \alpha_r W_r$ describes the production
of ice in all thickness categories thinner than h per unit of strain.
The coefficient α_o is the amount of open water produced per unit of
strain.

Observations of the redistribution of the Beaufort Sea ice cover
indicate that a reasonable form of $\alpha_o(\theta)$ is that presented in Figure 3.2
(Rothrock and Hall, 1975). Therefore, open water is produced not only
during opening deformations $(0 \le \theta < \pi/2)$ but also during shearing
deformations that close up the ice slightly $(\pi/2 < \theta \le 2\pi/3)$. The

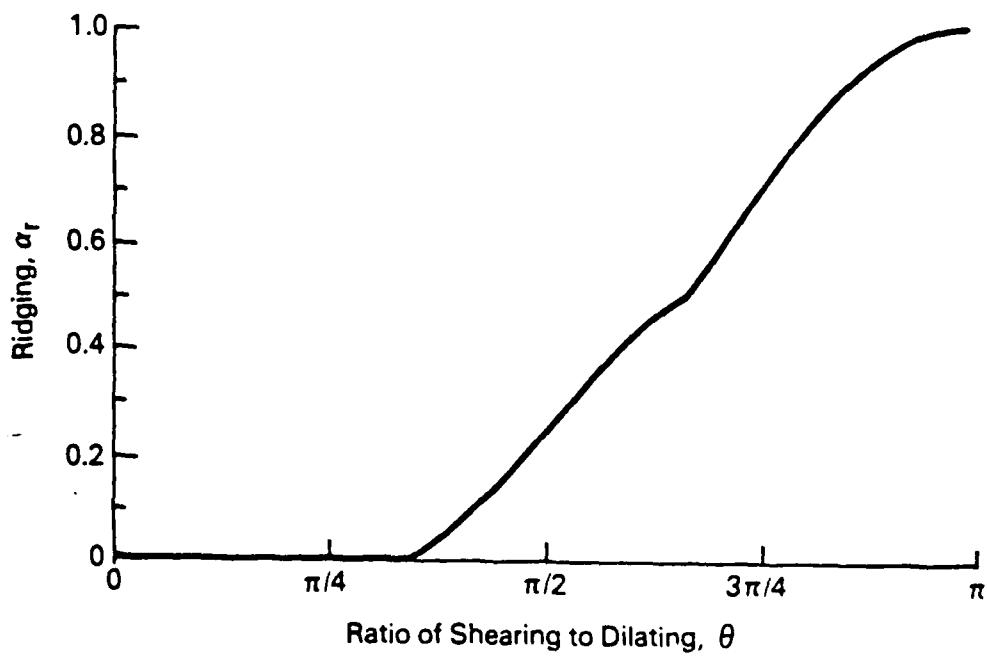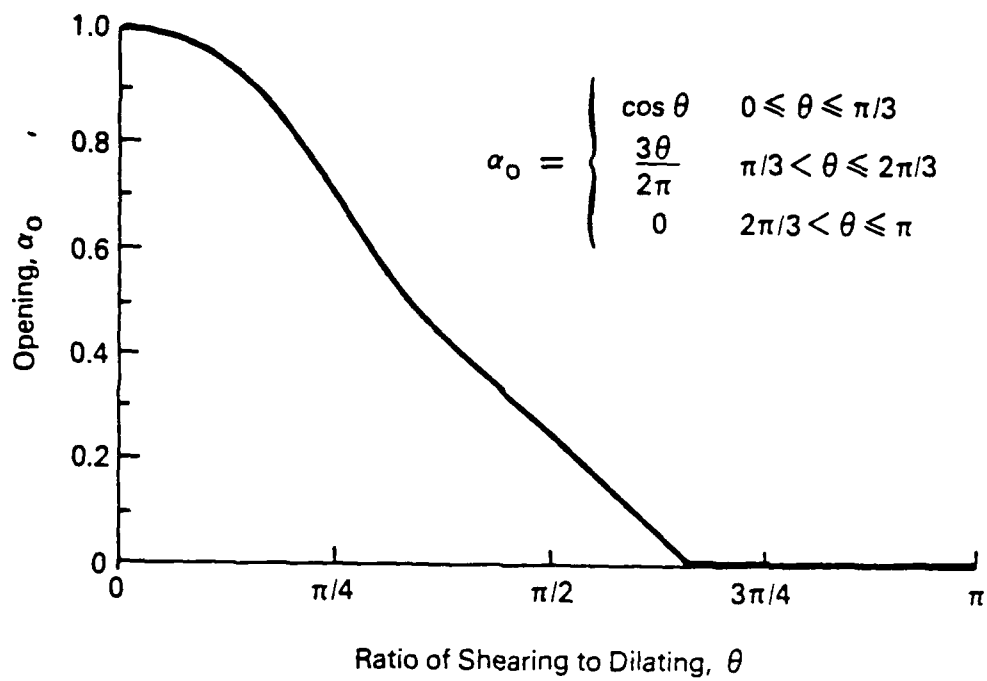$$\alpha_o = \begin{cases} \cos \theta & 0 \leqslant \theta \leqslant \pi/3 \\ \dfrac{3\theta}{2\pi} & \pi/3 < \theta \leqslant 2\pi/3 \\ 0 & 2\pi/3 < \theta \leqslant \pi \end{cases}$$

Figure 3.2.   Opening and Ridging Apportioners

31

function α_o is monotonic decreasing, indicating that more open water is formed during opening than during closing deformations, a result obviously compatible with physical intuition.

The production of ice per unit strain in all categories thinner than h is $\alpha_r W_r$, which describes the production of ice from ridging. The coefficient $\alpha_r(\theta)$, like $\alpha_o(\theta)$, depends on the relative amounts of shearing, opening and closing. Several properties of α_r are important: α_r is positive because unridging cannot occur; α_r is monotonic increasing, indicating that more ridging occurs during closing than during opening deformations; and finally,

$$\alpha_o(\theta) - \alpha_r(\theta) = \cos\theta \qquad (3.15)$$

to satisfy conservation of area.

Following Thorndike et al. (1975), ridging is described by

$$n(h_2) = \int_0^\infty \gamma(h_1, h_2)\, a(h_1)\, dh_1 \quad , \qquad (3.16)$$

where $a(h_1)$ is the fraction of the area covered by ice of thickness h_1 per unit thickness that participates in the ridging process and $n(h_2)$ is the fraction of the area of ice of thickness h_2 per unit thickness that is produced by the ridging process. The function $\gamma(h_1, h_2)$, called the ridging process, is the distribution of thicknesses produced by ridging of a unit area of ice of thickness h_1 . The infinite limit of integration is strictly formal in that the integral is always zero at all thicknesses $h_1 > h_{max}$, the thickest ice present. The ridging mode W_r is formed by combining production of all thinner categories while accounting for loss of ice that participates in the ridging process. Therefore,

$$W_r(h) = \int_0^h \left[n(h_2) - a(h_2) \right] dh_2 \Big/ W_r(\infty) \quad , \qquad (3.17)$$

32

where $W_r(\infty)$ is introduced to conserve total area. Additional important general properties of the redistribution function may be found in Thorndike et al. (1975). Specific choices used in the simulation are now presented.

The ridging process is chosen to reflect the assumption that all ridged ice is k times its original thickness. Thus,

$$\gamma(h_1, h_2) = \frac{1}{k} \delta(h_2 - kh_1) \quad . \tag{3.18}$$

Although ice produced by ridging surely is in a distribution of categories, the assumption that ice of thickness h_1 is always ridged into ice of thickness $h_2 = kh_1$ is attractive for its simplicity. The value $k = 15$ is used based on the results of Parmerter and Coon (1972). The AIDJEX model (Coon et al., 1974) used $k = 5$, which is now thought to be too low. Different forms of ridging processes have been assumed by Bugden (1979) and more recently by Hibler (to appear). There are few data available to test these assumptions.

The participation function $a(h)$ describes the fraction of area covered by ice of thickness h that is converted by the ridging process. This function is bounded above by the fraction of area covered by ice of thickness h that is present. Therefore, it is useful to assume that

$$a(h) = b \left[G(h) \right] g(h) \quad , \tag{3.19}$$

where $g = \frac{\partial G}{\partial h}$ and $g(h)$ dh is the fraction of area covered by ice thinner than $h + dh$ and at least as thick as h (Thorndike et al., 1975). The function b is the fraction of ice present that participates in the ridging process. The function b (Figure 3.3) is assumed zero for the thinnest G_o-th percentile, which is assumed not to be available for ridging. In a sense we protect this thinnest ice, assuming that it lies in the openings between irregular, large, thick floes and cannot be ridged without fracturing the thicker ice. This has the effect of shifting curve b to the right in Figure 3.3. It is also assumed that the function b decreases with increasing values of G. That is, less

33

of the thicker ice is available for ridging. For simplicity, the decrease is linear up to the G_1-th percentile and then constant up to the G_*-th percentile. The small amount of thicker ice available for ridging ($G_1 < G \le G_*$) acknowledges the fact that some thick ice is fractured and piled into ridges. In Figure 3.3, constants have been chosen as $G_o = 0.05$, $G_2 = 0.20$, $G_* = 0.55$, and $B_o = 0.90$.
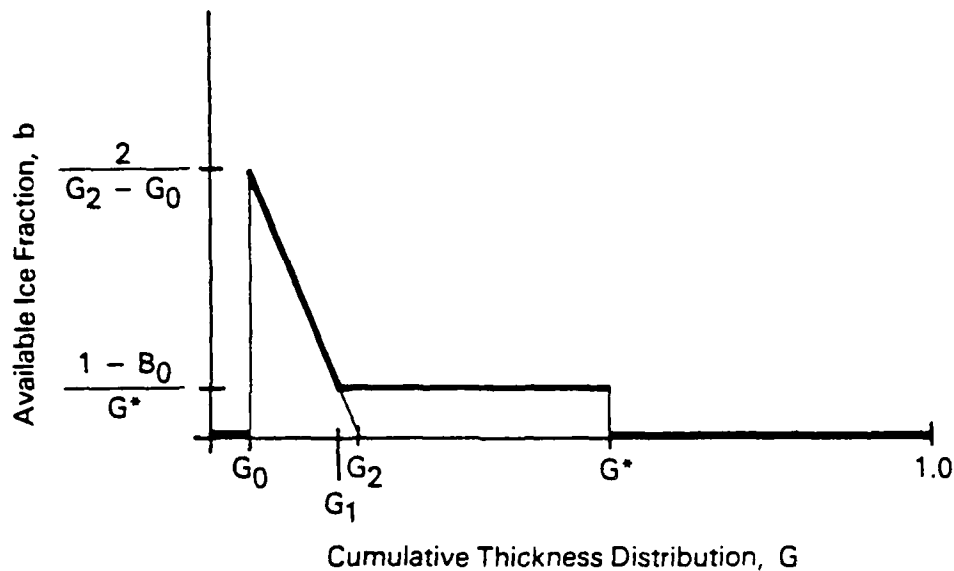

Figure 3.3.   Fraction of Ice in Each Thickness Category Available for Ridging

The rate at which energy is dissipated by the deforming ice cover was originally related to the changes in gravitational potential energy caused by mechanical deformation p_p and to the frictional loss in ridging p_f. In the modified formulation we introduce another energy sink p_s to account for energy dissipated by shearing deformations that do not alter the ice thickness distribution.

Analysis of each of the first two energy sinks provides a similar relationship. From the gravitational potential energy changes (Rothrock, 1975),

$$p_p = c_p \int_0^\infty h^2 \frac{\partial \psi}{\partial h} \, dh \quad , \tag{3.20}$$

34

where $c_p = \frac{1}{2} \hat{\rho} g$ and $\hat{\rho} = \frac{\rho}{\rho_w} (\rho_w - \rho)$. By substituting the assumed redistribution Ψ , this becomes

$$P_p = D_p \alpha_r p_p^* \quad , \tag{3.21}$$

where

$$p_p^* = c_p \int_0^\infty h^2 \frac{\partial W_r}{\partial h} \, dh \quad . \tag{3.22}$$

The loss due to friction has been analyzed and estimated, and the functional form is the same as for potential energy changes (Rothrock, 1975):

$$P_f = D_p \alpha_r p_f^* \quad , \tag{3.23}$$

where

$$p_f^* = c_f \int_0^\infty \frac{h^2 a(h)}{1 - (1/k)} \, dh \tag{3.24}$$

and

$$c_f = \frac{\mu' (\rho_w - \rho) \, g}{2 \tan \phi'} \left[\frac{\rho(k - 1)}{\rho_w} \right]^2 \quad , \tag{3.25}$$

where μ' is the coefficient of sliding friction and the angle ϕ' is the slope of keels of pressure ridges.

To determine the material constants c_p and c_f , mass densities and the gravitational constant $g = 9.80 \text{ m/s}^2$ are used. The coefficient of sliding friction is $\mu' = 0.35$, a slight increase from early AIDJEX model calculations. The increase is an attempt to increase yield strength to values found to be necessary for simulating observed ice motions accurately. This value is within the range of reasonable values, but there are no data to support the choice of any particular value in the ridging process. We have retained the value of about 39° for the angle ϕ' ; therefore, $\tan \phi' = 0.8$.

The contributions from p_p and p_f are combined in the one expression

$$P_p + P_f = D_p \alpha_r p^* \quad , \tag{3.26}$$

where $p^* = p_p^* + p_f^*$ may be written as

$$p^* = c^* \int_0^\infty h^2 a(h) \, dh \tag{3.27}$$

35

and

$$c^* = \frac{1}{2} \hat{\rho} g k \left[1 + \frac{\mu'}{\tan \phi'} \frac{\rho}{\rho_w} (k - 1) \right] \ . \tag{3.28}$$

For the chosen material constants, we find that

$$c^* = 43 \times 10^3 \ \text{N/m}^3 \ . \tag{3.29}$$

The energy dissipated by friction is about 5.5 times as large as the energy dissipated by potential energy changes. Early AIDJEX model calculations neglected friction and had a very weak strength as a result.

The final energy sink has not been analyzed to determine how shearing dissipates energy. We assume the process to be rate independent so that P_s is linear in D_p, the rate of plastic deformation, and write

$$P_s = D_p q \ , \tag{3.30}$$

where q is the rate of dissipation of energy per unit deformation rate. It may depend on the ratio of shearing to dilating, the thickness distribution and the stress state. By considering the relative motion of ice on either side of a velocity discontinuity, it is easy to imagine that q varies as the product of the ice pressure $(-\sigma_I)$ and a coefficient $\alpha_s(\theta)$. Then,

$$q = -\sigma_I \alpha_s \ , \tag{3.31}$$

but we do not make a direct use of this assumption. Rather, we find q as a residual in the energy balance. The requirement that q be nonnegative introduces a weak restriction on our choice of yield surface shape.

When we equate stress power to rate of energy dissipation so that

$$P_\ell = P_p + P_f + P_s \ , \tag{3.32}$$

this mechanical energy balance equation provides a definition of the shearing dissipation q for all plastic stress and stretching states. We find that

$$\frac{q}{p^*} = \left(\frac{\sigma_I}{p^*} \right) \cos \theta + \left(\frac{\sigma_{II}}{p^*} \right) \sin \theta - \alpha_r(\theta) \ . \tag{3.33}$$

The shearing dissipation depends only on θ for a given yield surface and flow rule. For the triangular yield surface and normal flow rule as well as the chosen ridging coefficient α_r, the shearing dissipation is shown in Figure 3.4. The shearing sink is never negative, a condition necessary to prohibit energy generation. It is seen that energy is dissipated in shearing when $\pi/4 < \theta < 3\pi/4$ and zero outside this range. The value of q/p^* has a maximum of 0.25. The shearing dissipation is an important addition to the constitutive law. With the addition of a shear dissipation sink, less open water is formed during shearing, and this fact prevents or reduces softening of the model behavior in many deformations. This results in larger values of strength in comparison with values produced by the early AIDJEX model.
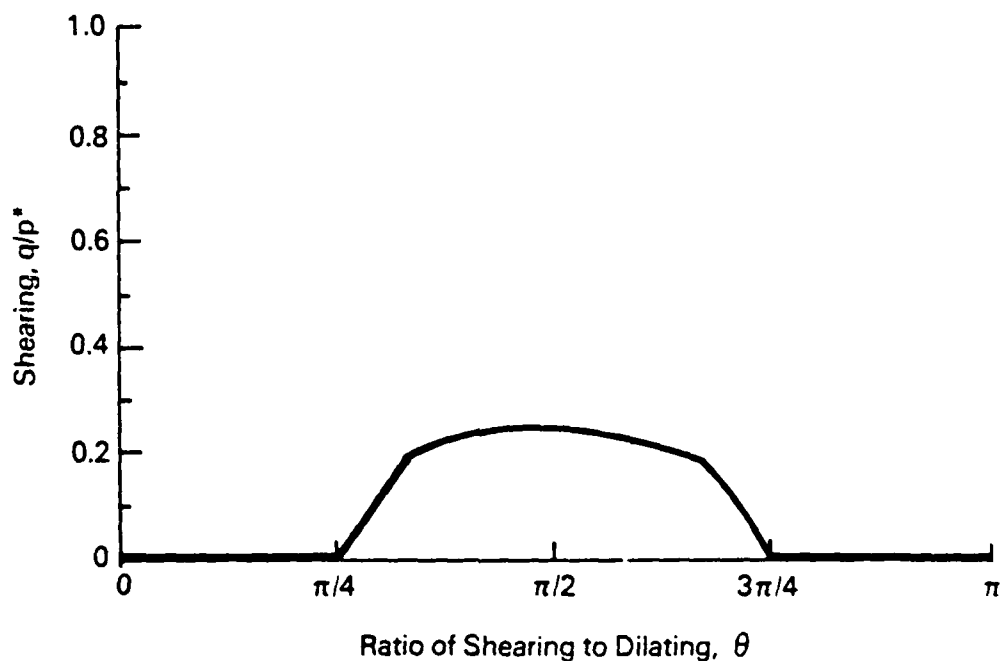
Figure 3.4. Relative Amount of Shearing Dissipation Without Redistribution

37

Chapter 4
INPUT DATA REQUIREMENTS

4.1 FREE-DRIFT

At each location at which ice velocity is to be calculated, the free-drift model requires that the geostrophic wind velocity and deep ocean current velocity be specified. The geostrophic wind can be replaced by the surface wind if the drag coefficient c_a and turning angle α are changed appropriately. In addition, the mass area density of the ice cover m is needed. Daily average values of wind and current velocities are appropriate so that ice motion trajectories are built up by vector summation of day-to-day displacements.

An individual oil spill trajectory may be calculated by inputting wind and current vectors at the location of the spill each day. However, if a general capability is needed for following any oil spill in a region, e.g., the southern Beaufort Sea, then the wind and current fields are needed everywhere in the region. To date, the only ocean current information available is the steady geostrophic ocean current field determined from the dynamic sea surface topography.

When a prediction is required, winds and currents must also be predicted out to the verifying time. The best geostrophic wind predictions are useful out to a maximum of about 5 days. When model simulations are made in a hindcast mode for the sake of determining the present location of an oil spill that cannot be observed directly, then this predictive time limitation does not apply.

The free-drift velocity is relatively insensitive to the mass area density (or mass density ρ times mean thickness $\bar{h}$). Therefore, it is adequate to consider only climatological changes in it. In this case, no data are required.

38

4.2 COMPLETE ICE DYNAMICS MODEL

Since the internal ice stress transmits forces horizontally through the ice cover, ice velocity at one location can be sensitive to driving forces at another location. Therefore, the complete ice dynamics model requires that geostrophic wind and current fields be input over the entire region of the calculation. These fields (the geostrophic ocean current is steady state) can vary continuously in time to allow smooth transitions during numerical integration, but time histories should be filtered to remove all frequencies with periods shorter than 1 day. Barometric pressure fields at synoptic intervals (6 hours) fill this need adequately.

Calculating ice motions within a region requires that either ice velocity, traction (the traction vector describes the normal and shear force applied to the ice edge) or a combination of the two vectors be specified everywhere around the boundary.

At those boundaries that lie along shorelines, the ice motion is assumed to be zero. Slippage of the ice along the shoreline is automatically calculated by the model as a plastic flow within the ice nearest shore. Along those boundaries corresponding to a free ice edge, the traction can be prescribed to be zero. Since the model calculates motion of the ice, this ice edge is automatically followed. Neither of the above boundary conditions requires input of observations.

When the region of interest is bounded by a line lying within the interior of the ice cover, either the velocity or traction along the line is required. For a hindcast calculation, data buoys can be deployed to provide such input data. This method has been used in the past (e.g., Pritchard, 1981). Another possible aproach is to extend the region of interest to a coastal boundary or a free ice edge. This solution, however, increases the requirement for additional wind and current data and can introduce substantial errors if these driving forces are known

only poorly. Although Pritchard and Thomas (1980) show that errors in calculated ice velocity decay rather strongly with distance from the boundary, the question of how to specify conditions at a boundary within the ice cover remains an open research question at this time.

For a forecast calculation, the boundary velocity must be predicted. One approach in predicting the boundary velocity is to assume persistence and to input the last known values after forward extrapolation. Free-drift predictions could also be used as boundary velocities, but the level of performance of the complete model then is degraded and at times is no better than the free-drift model (Coon et al., 1977).

Finally, initial conditions require that the thickness distribution, velocity and stress be specified everywhere. The latter two variables have little long-lasting effect on response and can be input as nominal values, say $\underset{\sim}{v}_o = \underset{\sim}{0}$, $\underset{\sim}{\sigma}_o = -\frac{p^*}{2}\underset{\sim}{1}$, where $\underset{\sim}{v}_o$ and $\underset{\sim}{\sigma}_o$ are initial values of $\underset{\sim}{v}$ and $\underset{\sim}{\sigma}$. But the initial thickness distribution affects behavior for several weeks typically. The thicker ice concentrations, say thicker than 1.5 m, can be input from climatological values. The thin ice requires that satellite or aircraft imagery be obtained to determine the ice compactness and the concentrations of thin ice in several categories. A combination of visual, infrared, radar and microwave sensors is useful to provide all weather coverage and to identify the various categories needed.

Chapter 5

MODEL PERFORMANCE

5.1 DEFINITION OF ERRORS

An evaluation of the free-drift and complete ice dynamics models requires some test of their accuracy in predicting observed motions (Thorndike and Cheung, 1977). Output from these models is in the form of daily velocity vectors. Velocities are integrated to produce trajectories. For comparison, the actual observed trajectories are differentiated to produce daily velocity vectors. The vector difference between these and the model velocities is the error measure used.

Daily error vectors exhibit a good deal of variability. In order to predict the error expected in using one of the models, variance ellipses have been constructed. These give an area within which the error vector is expected to lie, at some confidence level, for each geographic location where a time-series comparison is available.

Computation of the mean error and standard deviation of the error follows standard statistical definitions. We let $\underset{\sim}{v}$ be the calculated daily velocity and $\underset{\sim}{w}$ be the observed daily velocity. Although no sub- or superscript is used, each variable is evaluated daily. The daily velocity error is

$$\underset{\sim}{\varepsilon} = \underset{\sim}{v} - \underset{\sim}{w} \ . \tag{5.1}$$

During 1 month, the mean error is

$$\overline{\underset{\sim}{\varepsilon}} = \frac{1}{N} \sum \underset{\sim}{\varepsilon} \ , \tag{5.2}$$

where N is the number of daily observations during the month. The standard deviation of the error is

$$S_\varepsilon = \left(\frac{1}{N-1} \sum |\underset{\sim}{\varepsilon} - \overline{\underset{\sim}{\varepsilon}}|^2 \right)^{\frac{1}{2}} \ . \tag{5.3}$$

Because of large errors in current velocities $v_{\sim g}$, it is useful to isolate the effect on total daily error $\underset{\sim}{\varepsilon}$. This separation is useful when different error measures represent errors from different physical processes. To this end, we introduce the relative ice velocity $\underset{\sim}{G}$ by separating the geostrophic current $v_{\sim g}$:

$$\underset{\sim}{v} = \underset{\sim}{G} + v_{\sim g} \quad . \tag{5.4}$$

Then the error, mean error and standard deviation actually computed are

$$\underset{\sim}{e} = \underset{\sim}{G} - \underset{\sim}{w} \tag{5.5}$$

$$\overline{\underset{\sim}{e}} = \frac{1}{N} \sum \underset{\sim}{e} \tag{5.6}$$

$$S_e = \left(\frac{1}{N-1} \sum \left| \underset{\sim}{e} - \overline{\underset{\sim}{e}} \right|^2 \right)^{\frac{1}{2}} \quad . \tag{5.7}$$

Combining Equations (5.1), (5.4) and (5.5), we obtain

$$\underset{\sim}{\varepsilon} = \underset{\sim}{e} + v_{\sim g} \quad , \tag{5.8}$$

and it follows that when geostrophic ocean currents are included in calculating the ice drift, the mean daily error is

$$\overline{\underset{\sim}{\varepsilon}} = \overline{\underset{\sim}{e}} + \overline{v_{\sim g}} \tag{5.9}$$

and the standard deviation of the error $\underset{\sim}{e} + v_{\sim g}$ is

$$S_\varepsilon = \left(S_e^2 + S_{v_g}^2 + 2 \operatorname{cov}(\underset{\sim}{e}, v_{\sim g}) \right)^{\frac{1}{2}} , \tag{5.10}$$

where the covariance is bounded as

$$-S_e S_{v_g} \leq \operatorname{cov}(\underset{\sim}{e}, v_{\sim g}) \leq S_e S_{v_g} \quad . \tag{5.11}$$

42

When ocean currents are constant along the month-long trajectory, or nearly constant, then $\underset{\sim}{v}_g$ satisfies

$$\underset{\sim}{v}_g \approx \overline{\underset{\sim}{v}}_g \quad \text{and} \quad S_{v_g} \approx 0 \quad . \tag{5.12}$$

The standard deviation of daily errors $\underset{\sim}{\varepsilon}$ becomes

$$S_\varepsilon = S_e \quad . \tag{5.13}$$

If $\underset{\sim}{v}_g$ does vary, the standard deviation of the daily error, using Equations (5.10) and (5.11), is found to be bounded by

$$S_\varepsilon \leq S_e + S_{v_g} \quad , \tag{5.14}$$

which shows the range of influence that ocean current variations may have on the standard deviation of errors S_ε .

Variance ellipses are constructed as follows. Rectangular coordinates are used to avoid difficulties inherent in working with azimuths. The variance-covariance matrix at each point for each month is also computed:

$$\underset{\sim}{S} = \begin{pmatrix} S_x^2 & S_{xy} \\ S_{xy} & S_y^2 \end{pmatrix} \tag{5.15}$$

where

$$S_x^2 = \frac{1}{N-1} \sum (x-\overline{x})^2$$

$$S_y^2 = \frac{1}{N-1} \sum (y-\overline{y})^2$$

$$S_{xy} = \frac{1}{N-1} \sum (x-\overline{x})(y-\overline{y}) \quad .$$

A bivariate normal distribution has the probability density function

$$f(x,y) = \frac{1}{2\pi S_x S_y \sqrt{1-r^2}} e^{-Q/2} \tag{5.16}$$

where

$$Q = \frac{1}{(1-r^2)} \left[\frac{(x-\bar{x})^2}{S_x^2} - \frac{2r(x-\bar{x})(y-\bar{y})}{S_x S_y} + \frac{(y-\bar{y})^2}{S_y^2} \right] \qquad (5.17)$$

with the mean $(\bar{x}, \bar{y})$ and correlation $r = S_{xy}^{\frac{1}{2}}$.

The locus of $Q = c^2$ (c is constant) defines an equiprobability ellipse. The probability p that a random point on the x-y plane will fall within the ellipse is

$$p = 1 - e^{-c^2/2} \qquad . \qquad (5.18)$$

The probability that the magnitude of the error vector lies within the range defined by the standard deviation is $p = 0.683$. This corresponds to a value of $c = 1.515$. Values of c for $p = 0.50$, 0.90 and 0.99 are respectively 1.177, 2.146 and 3.035. The variance ellipses plotted represent one standard deviation or $p = 0.683$. Values of c determine the size of the ellipse, so the given values may be used to scale ellipses at different probability levels.

A transformation of variables is made to simplify locating the equiprobability ellipses. Morrison (1976), among others, has described the procedure. First, a translation is made and a new coordinate system is defined as

$$\underset{\sim}{x} = \underset{\sim o}{x} - \underset{\sim o}{\bar{x}} \qquad , \qquad (5.19)$$

where $\underset{\sim o}{x}$ refers to the original coordinates and $\underset{\sim}{x}$ now refers to the new coordinates. The mean in the new coordinate system is now $(\bar{x}, \bar{y}) = (0, 0)$.

The variance-covariance matrix $\underset{\sim}{S}$ is not affected by a linear transformation. The determinant equation

$$|\underset{\sim}{S} - \lambda \underset{\sim}{I}| = \underset{\sim}{0} \qquad (5.20)$$

44

is solved for the characteristic roots (or eigenvalues) λ_1 and λ_2, and the equation

$$(\underset{\sim}{S} - \lambda \underset{\sim}{I})\underset{\sim}{e} = 0 \qquad (5.21)$$

is solved for the characteristic vectors (or eigenvectors) $\underset{\sim}{e}_1^T = (\cos \alpha, \sin \alpha)$ and $\underset{\sim}{e}_2^T = [\cos (\alpha+\pi/2), \sin (\alpha+\pi/2)]$ where α is the angle the first principal axis makes with the x-axis. A rotation of coordinates gives

$$u = \underset{\sim}{x}^T \underset{\sim}{e}_1 \qquad (5.22)$$

$$v = \underset{\sim}{x}^T \underset{\sim}{e}_2$$

where the new vector components u and v are independent and uncorrelated with the variances

$$\sigma_u^2 = \lambda_1 \qquad (5.23)$$

$$\sigma_v^2 = \lambda_2 \quad .$$

In this last coordinate system, Equation (5.17) becomes

$$Q = \frac{u^2}{\lambda_1} + \frac{v^2}{\lambda_2} \quad , \qquad (5.24)$$

and when the substitution $Q = c^2$ is made we have

$$\frac{u^2}{c^2 \lambda_1} + \frac{v^2}{c^2 \lambda_2} = 1 \quad , \qquad (5.25)$$

which is the equation of an ellipse with major and minor axes of lengths $2c\sqrt{\lambda_1}$ and $2c\sqrt{\lambda_2}$, respectively.

The entire statistical procedure is coded in Fortran. Results from the various modeling runs are read from tapes and compared with observed trajectories on data cards. Positions of data stations do not always correspond to grid nodes in the model. For these cases, the node closest to the station is used as if they are the same point. Output includes trajectories for the complete ice dynamics model, the free-drift model and observed motion. Average velocity error vectors are computed from the difference in trajectories at the end of the period. The semimajor and semiminor axes of the variance ellipses are given with their orientation. Standard deviations are also computed.

5.2 RESULTS OF SIMULATIONS

The free-drift and complete ice dynamics models have been tested against observed ice motions during four periods. During the AIDJEX experiment, manned camps and data buoys were used to track motion of pack ice in the Beaufort Sea. Observations were made from April 1975 to May 1976 on at least a daily basis. From these observations, four time periods are chosen to test the models: 13-28 April 1975 (75RUN2B), 17-25 May 1975 (75RUN1F), 27 January through 12 February 1976 (76RUN5C) and June through December 1975. A free-drift calculation using the same input data is made for each run. No changes are made in the free-drift calculation from run to run.

5.2.1 75RUN2B: 13-28 April 1975

Only the position of the Big Bear camp (BB) is available for this calculation. The modeled area, Figure 5.1, extends from Banks Island to Point Barrow in a roughly rectangular area. The boundary is constrained to be motionless alongshore and to follow free-drift along the outer grid nodes. Ice strength is determined by ice thickness distribution. An initial distribution was estimated from NOAA satellite images. As the ice deforms, the thickness distribution changes causing hardening or softening. Thermal growth of ice during the period of the experiment was included in the thickness distribution. The ice strength varies from $p^* \simeq 5 \times 10^3$ N/m to 1×10^4 N/m . These strengths
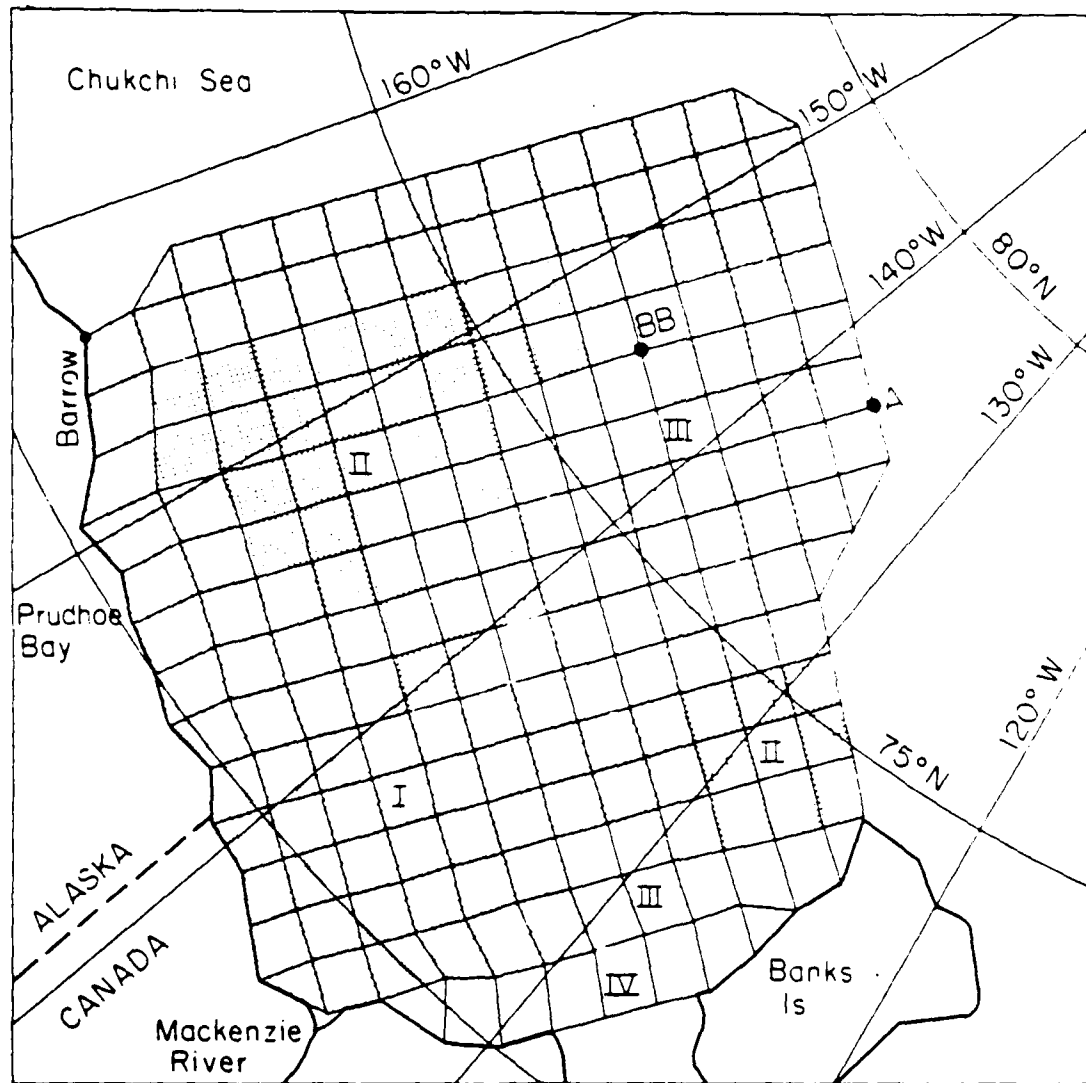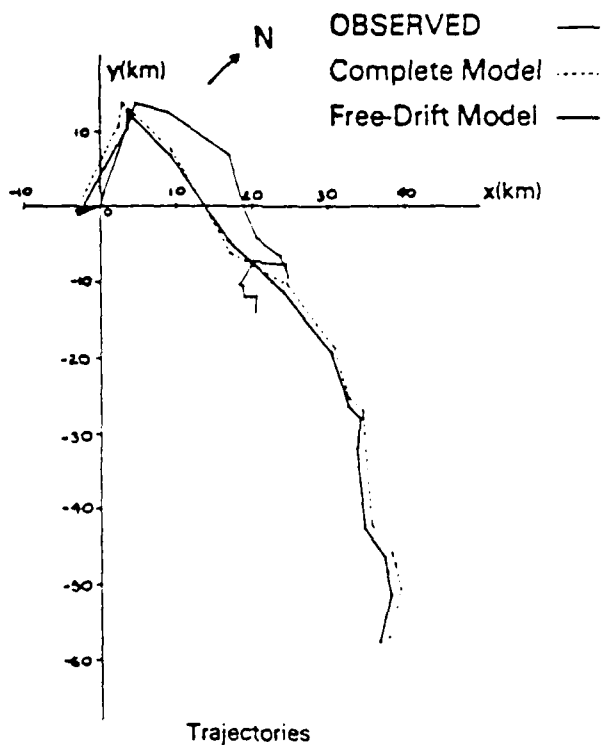
46

Figure 5.1. Region Modeled in 75RUN2B. Location of Big Bear (BB) Is Shown on 11 April 1975. [Shaded Regions Identified by Roman Numerals Were Used by Coon et al. (1977) to Describe Different Ice Conditions.]

are too low to represent large-scale strength accurately. During this time, a low pressure system moves eastward across the Beaufort Sea at ~200 km/day. This system gives rise to a moderately strong air stress of ~0.2 Pa (1 Pa = 1 N/m^2) near Big Bear. Further details of this experiment are given by Coon et al. (1977).

Figure 5.2 shows observed and simulated trajectories for the Big Bear camp from 13 through 28 April 1975. The actual trajectory is shown along with a trajectory produced by the free-drift model and one produced by the complete ice dynamics model (the early AIDJEX model is used for the complete model in this simulation). For this computer run, 75RUN2B, the strength input to the AIDJEX model is so low that it behaves very similarly to the free-drift model. Both models track the actual motion very well during the first 7 days of the trajectory. On the eighth day, the camp slows and begins an erratic motion while the models predict continued motion to the southeast. During the first 3 days, the motion is offshore to the northeast. Then a steady southeast motion begins which tends to pile the ice into the shore of Banks Island. By the seventh day the effect of compressing the ice against shore reaches Big Bear. The strength of the ice is sufficient to prevent any further motion, and the wind remains more or less steady. The free-drift model does not account for ice strength and thus predicts continued motion. The strength in this version of the complete ice dynamics model is so low as to be insignificant and it too allows continued motion to the southeast.

These trajectories were used to calculate a mean velocity error vector. This is simply the error in the trajectory after 15 days divided by the total time. Variance ellipses are calculated, see Figure 5.2, for the variance in daily velocity error vectors about the mean error vectors. The ellipses represent the region in which 68.3 percent of daily velocity error vectors are expected to fall. The elongation of the variance ellipses is probably caused by the prevalent motion in the direction of the elongation. The variance is equal to the sum of the squares of the major and minor axes of the ellipse. The standard deviation is given along with daily velocity error vectors in Table 5.1.

48

OBSERVED ———
Complete Model ·····
Free-Drift Model ———

Trajectories

Free-Drift Error Vector
and Variance Ellipse

Model Error Vector
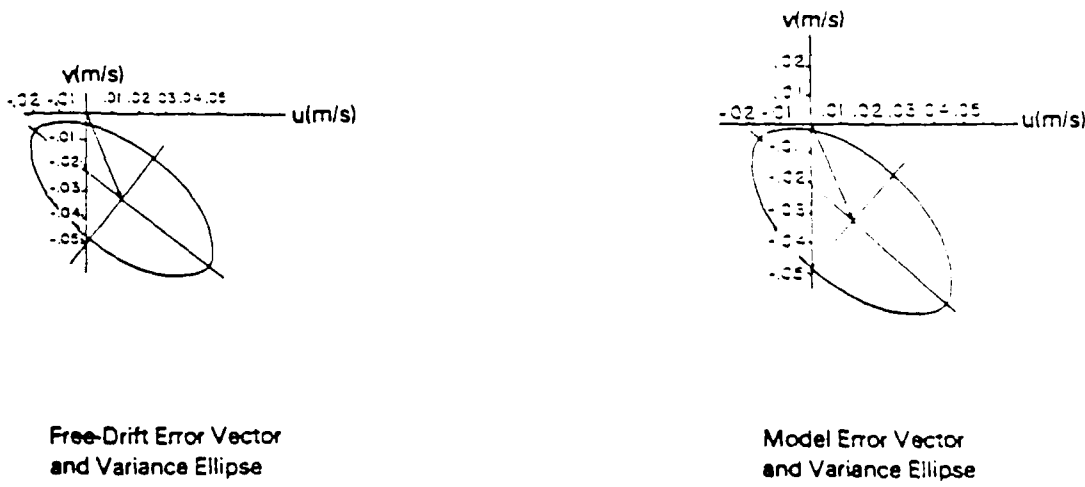and Variance Ellipse

Figure 5.2.   Ice Trajectory at Big Bear During 13-28 April 1975 (75RUN2B)

TABLE 5.1. ERROR STATISTICS FOR COMPLETE ICE DYNAMICS AND FREE-DRIFT MODELS (x, y)

| | | Complete Ice Dynamics Model | | Free-Drift Model | |
Station	Location*	Error Vector ε_x , ε_y (m/s)	Standard Deviation (m/s)	Error Vector ε_x , ε_y (m/s)	Standard Deviation (m/s)
75RUN2B (13-28 April 1975)					
0(BB)	CAB	0.014, -0.032	0.046	0.012, -0.033	0.046
75RUN1F (17-25 May 1975)					
0(BB)	CAB	-0.003, 0.006	0.018	0.002, 0.0005	0.016
1(Ca)	CAB	0.0002, 0.0016	0.016	-0.003, 0.008	0.019
2(BF)	CAB	-0.004, 0.001	0.020	-0.012, -0.016	0.021
3(SB)	CAB	-0.001, 0.003	0.017	0.013, 0.003	0.021
765RUN5C (27 Jan.-12 Feb. 1976)					
1(Ca)	CAB	0.003, 0.002	0.027	-0.028, 0.015	0.092
2(BF)	CAB	-0.0005, 0.0004	0.027	-0.037, 0.0002	0.082
3(SB)	CAB	0.002, 0.0001	0.018	-0.024, 0.012	0.086
10	CAB	0.0003, 0.000	0.032	-0.027, 0.012	0.103
19	CAB	-0.0001, -0.0006	0.024	-0.043, -0.013	0.086
5	CAB	0.000, 0.0002	0.023	-0.039, -0.018	0.075
17	TRANS	0.000, 0.0001	0.046	-0.004, -0.001	0.106
14	TRANS	0.000, 0.0001	0.035	-0.019, -0.020	0.102
15	TRANS	0.006, -0.003	0.059	-0.017, 0.059	0.089
16	TRANS	0.009, 0.002	0.049	-0.022, 0.044	0.088
21	TRANS	-0.002, 0.016	0.038	-0.007, 0.028	0.092
20	NS	-0.007, 0.019	0.036	-0.002, -0.002	0.101
22	NS	-0.007, 0.017	0.035	-0.003, -0.004	0.108
23	NS	-0.008, 0.014	0.034	-0.009, -0.016	0.115

*CAB = Central Arctic Basin; TRANS = Transition Zone; NS = Nearshore Region.

50

5.2.2 75RUN1F: 15-25 May 1975

During this time, positions are available for four manned camps and six data buoys surrounding them (Figure 5.3). The four manned camps are designated Caribou (Ca), Big Bear (BB), Blue Fox (BF) and Snow Bird (SB). All the camps are on the ice pack of the central Arctic basin over 500 km offshore. Motions of the data buoys are used to provide boundary conditions for the AIDJEX model calculation and are not used in claculating trajectory errors. The time period for this comparison is chosen partly because of the availability of Landsat imagery, which provides an independent check of ice motions. A comparison of Landsat observed and modeled motions is given by Hall (1980). The ice is modeled as a perfectly plastic material with a constant (no hardening) uniaxial compressive strength of $p^* = 4 \times 10^4$ N/m . Further details on this model and the effect of strength are given by Pritchard (1978).

There are four manned camp trajectories available for comparison with 75RUN1F and free-drift model calculations. The trajectories are shown for the four manned camps in Figures 5.4 through 5.7. These cover the period from 17 to 25 May 1975. The motions are generally to the northwest for the first 3 days then they turn slowly to the southeast. This southeast drift motion of the camps is similar to that for the period of 75RUN2B. There is, however, no time when the camps stop moving for any length of time. This is reflected in the error and variance plots.

Both models track the camp motion fairly well, with the exception of the free-drift trajectory calculated for the Blue Fox camp (Figure 5.6). It is interesting to note that the orientation of the variance ellipses does not vary much from the northwest-southeast elongation. The magnitudes of error vectors and standard deviations are given in Table 5.1. Both the mean errors and standard deviations are smaller than for 75RUN2B, indicating that strength has some importance. This has been verified by Hall (1980) when comparing results of other simulations using lower values of strength (75RUN1E). In Hall's study, the constant strength
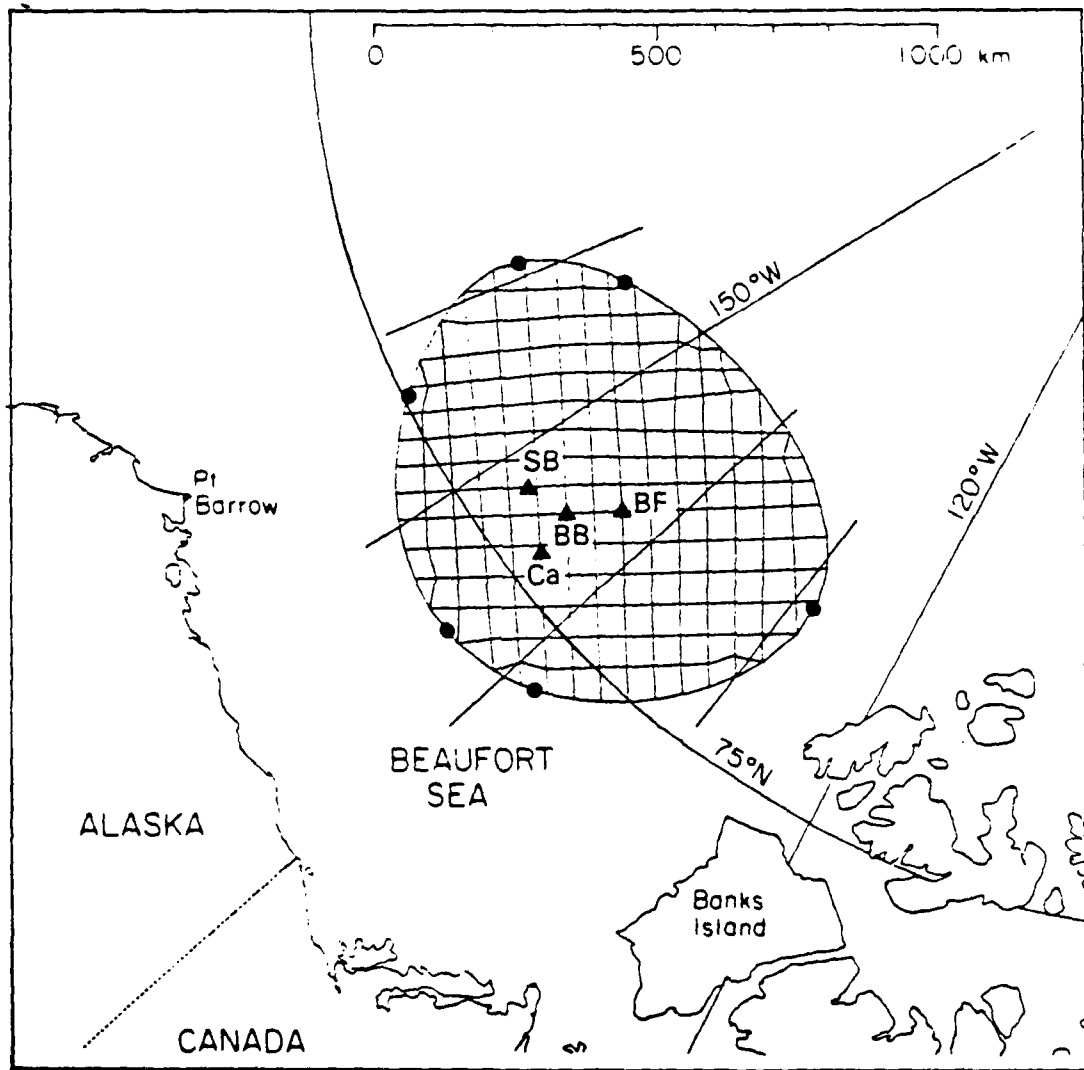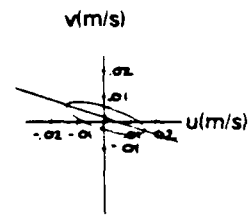
Figure 5.3. Region Modeled in 75RUN1F. Locations of the Caribou (Ca), Big Bear (BB), Blue Fox (BF) and Snow Bird (SB) Camps and the Six Data Buoys (Circles on Boundary) Are Shown on 15 May 1975.
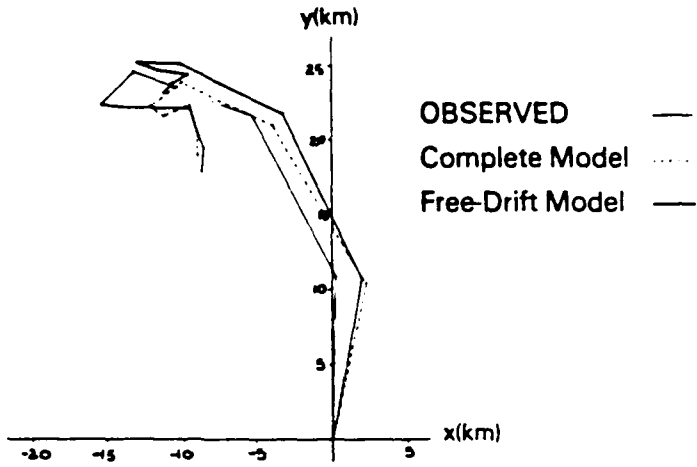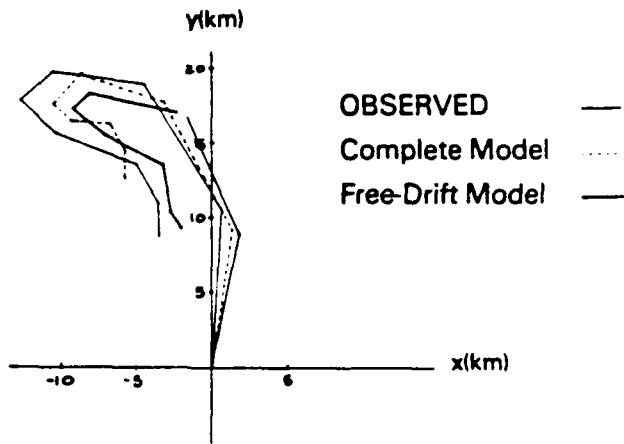
Trajectories
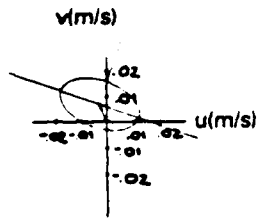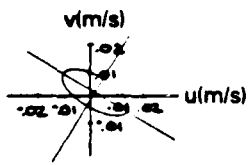

Free-Drift Error Vector
and Variance Ellipse

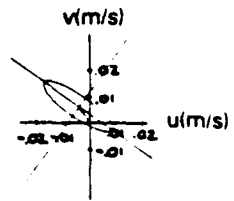Model Error Vector
and Variance Ellipse

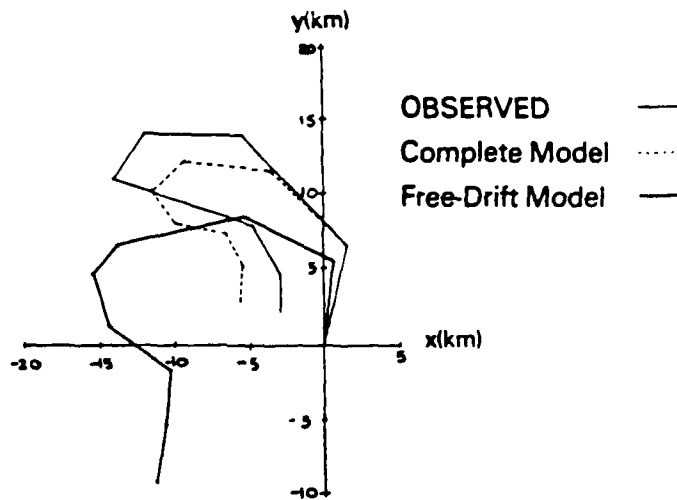**Figure 5.4.   Ice Trajectory at Caribou During 17-25 May 1975 (75RUN1F)**

Trajectories
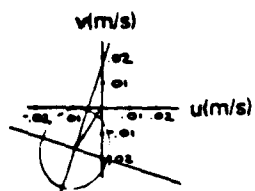

Free-Drift Error Vector
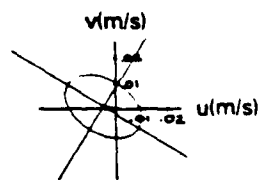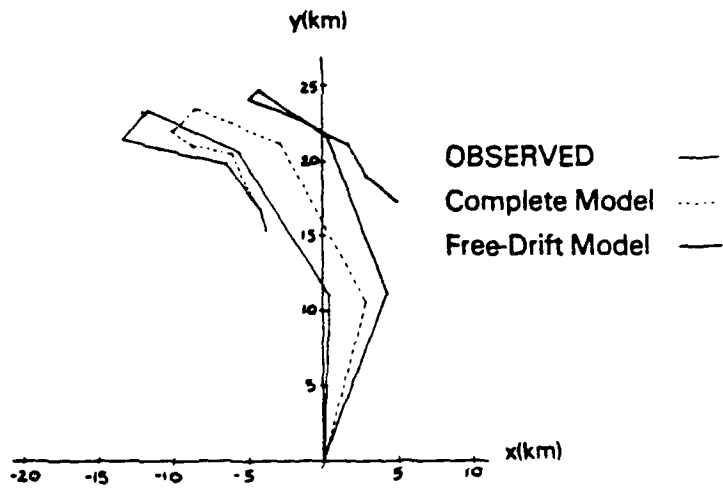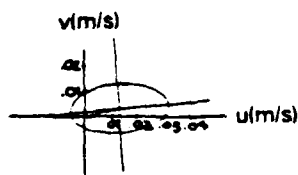and Variance Ellipse
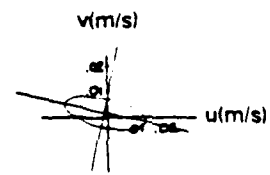

Model Error Vector
and Variance Ellipse

Figure 5.5.   Ice Trajectory at Big Bear During 17-25 May 1975 (75RUN1F)

Trajectories

Free-Drift Error Vector
and Variance Ellipse

Model Error Vector
and Variance Ellipse

Figure 5.6.   Ice Trajectory at Blue Fox During 17-25 May 1975 (75RUN1F)

Trajectories

Free-Drift Error Vector
and Variance Ellipse

Model Error Vector
and Variance Ellipse

Figure 5.7.   Ice Trajectory at Snow Bird During 17-25 May 1975 (75RUN1F)

AIDJEX model calculation is compared with Landsat data. He calculates a "figure of merit" from velocities for 1 day at 10 positions on the ice:

$$\Delta_d = \left(\frac{1}{N} \sum |\underset{\sim}{M} - \underset{\sim}{L}|^2 \right)^{\frac{1}{2}} \qquad (5.26)$$

where $\underset{\sim}{M}$ and $\underset{\sim}{L}$ are model and Landsat velocity vectors, respectively. The standard deviation is

$$S_E = \left(\frac{1}{N-1} \sum |\underset{\sim}{M} - \underset{\sim}{L}|^2 \right)^{\frac{1}{2}}, \qquad (5.27)$$

so

$$S_E = \left(\frac{N}{N-1} \right)^{\frac{1}{2}} \Delta_d , \qquad (5.28)$$

and for 10 cases, $N = 10$, $S_E = 1.054 \, \Delta_d$. Hall gives $\Delta_d = 1.4$ km/day corresponding to $S_E = 0.017$ m/s. This value compares well with our estimated S_E of 0.018 m/s for the 75RUN1F complete ice dynamics model calculation.

5.2.3 76RUN5C: 27 January Through 12 February 1976

In this last run, the complete ice dynamics model as described in Chapter 3 is used. Ice motions within the modeled region are monitored by three manned camps and eleven data buoys scattered throughout the region (see Figure 5.8). Boundary conditions are fixed along the shore from Banks Island to Point Barrow and constrained to follow the motions of five data buoys located around the outer nodes of the region. As in 75RUN2B, an ice thickness distribution is used to determine ice strength. The important difference is that the initial strength is two orders of magnitude higher, $p^* \simeq 10^5$ N/m. A more detailed discussion of the results that is provided here is presented by Pritchard (1981).

The period of this simulation is chosen because large temporal and spatial variations of air stress due to the passage of two storms were thought to provide a good test of the model under extreme conditions. Both strong onshore (compressive) and offshore (tensile) motions were
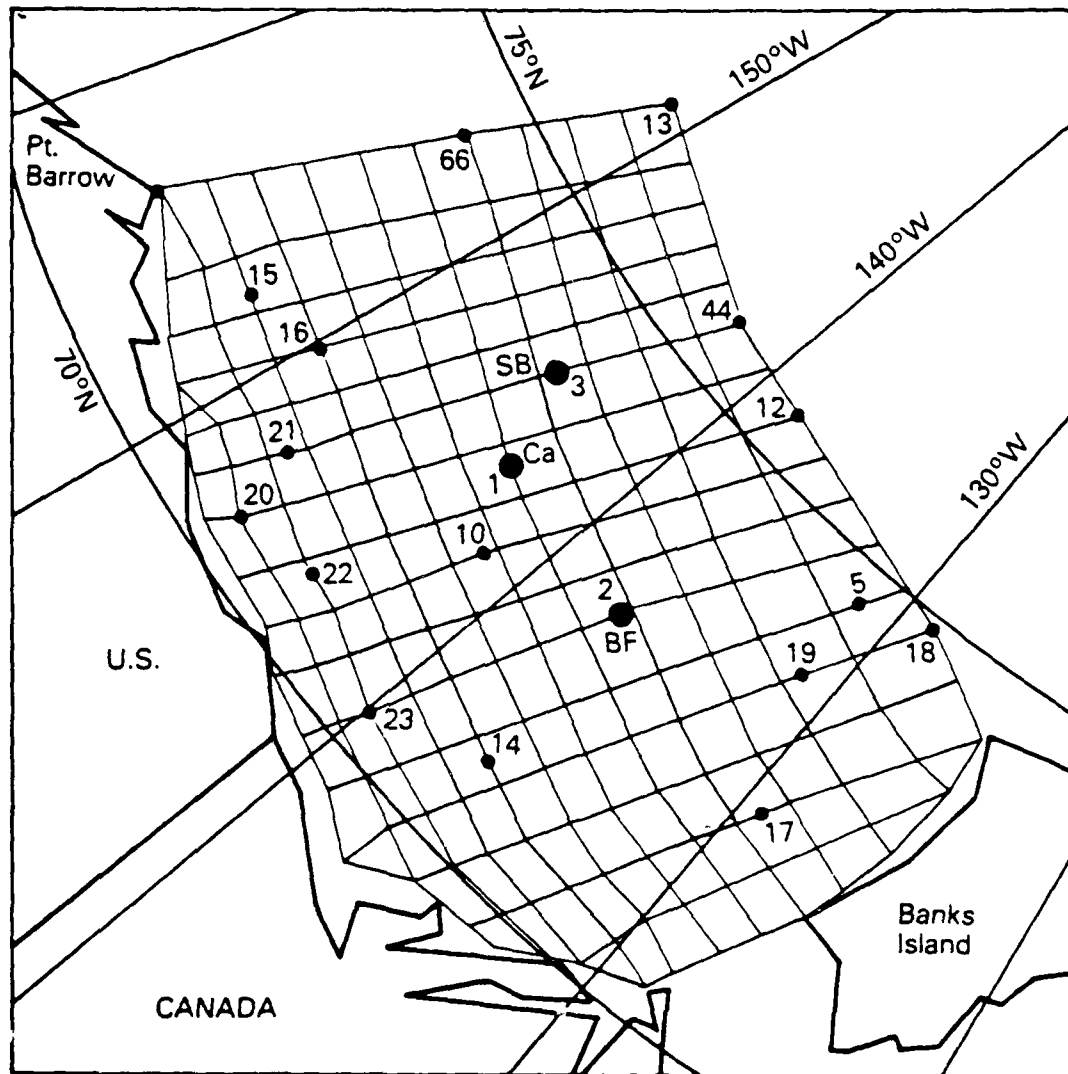
Figure 5.8. Region Modeled in 76RUN5C. Locations of the Caribou (Ca), Snow Bird (SB) and Blue Fox (BF) Camps and the Data Buoys (Small Numbered Circles) Are Shown on 27 January 1976.

58

observed as well as sharp discontinuities in ice motion giving rise to shearing in the stamukhi zone. High winds accompanying storms can cause large ice motions, because of the quadratic drag law, or no motion at all when the ice hardens.

Fourteen station trajectories scattered throughout the Beaufort Sea are available for comparison with simulated motions. Rather than present trajectories for all these stations here, four are chosen to represent distinct regions in the pack ice. (Table 5.1, however, includes the error statistics for all fourteen trajectories.) The Caribou manned camp (Ca) is located in the middle of the Beaufort Sea well into the central Arctic basin (see Figure 5.8). In the winter, this is a region of well-consolidated, uniform pack ice. Station 17 is a RAMS buoy located off the west coast of Banks Island. This is a region where large leads are continually opening and closing in response to the prevailing winds, which alternately drive the ice pack east and west. Station 20 is a RAMS buoy in the nearshore region. The ice in this area is relatively immobile compared to the rest of the pack because of the influence of the shoreline. The last region considered is the highly sheared stamukhi zone. This is the transition zone between the mobile ice pack and the fast ice nearshore. Station 16 is used to represent the motion in this region.

In each of the four comparisons, the motion predicted by free-drift is much larger than the observed motion. This is seen in both the trajectories and the variance ellipses in Figures 5.9 through 5.12. The period from 27 January to 12 February 1976 includes two large storms. The first of these drives the ice to the west; the second back to the east. For both storms, the free-drift calculations result in motions that are clearly too large. The resulting variance ellipses are quite large, with orientations roughly NNE to SSW and a maximum variance of about 0.10 m/s. The complete ice dynamics model does a much better job of predicting motions at this time of year. This is not surprising since the ice has considerable strength in the winter.
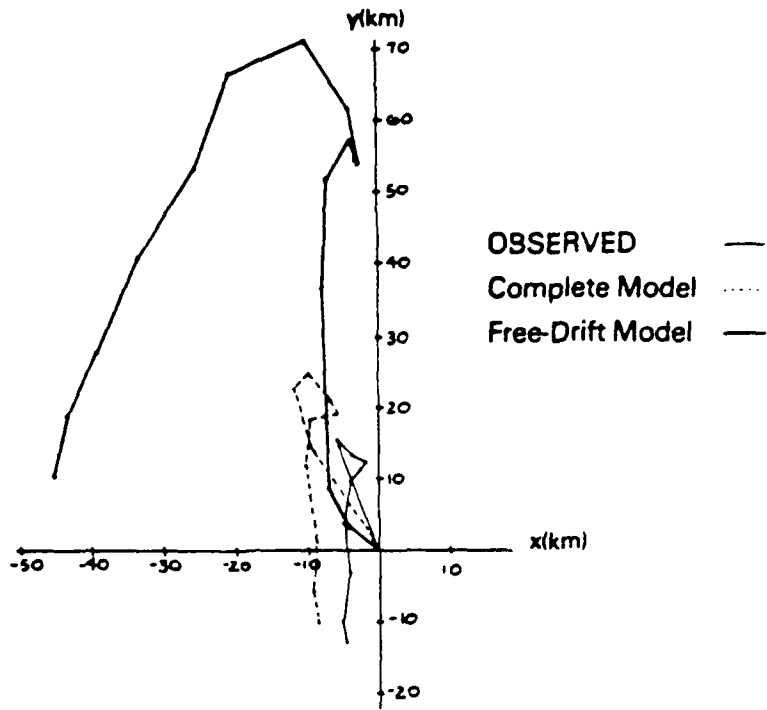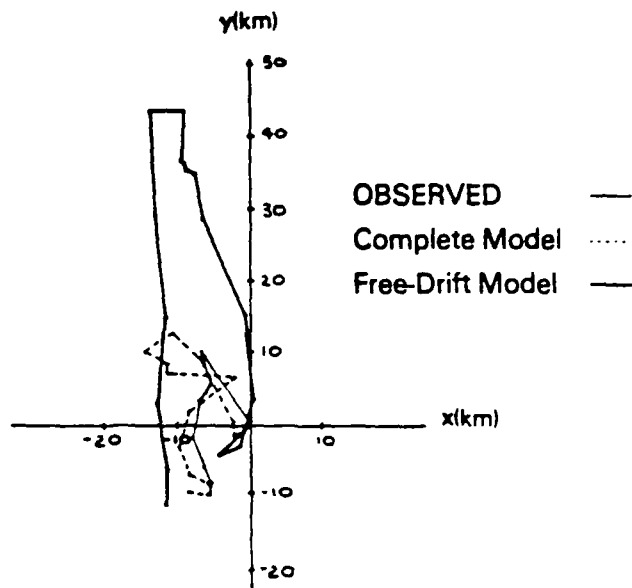
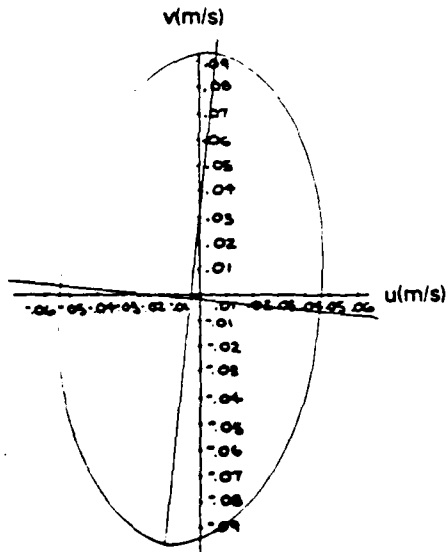Trajectories
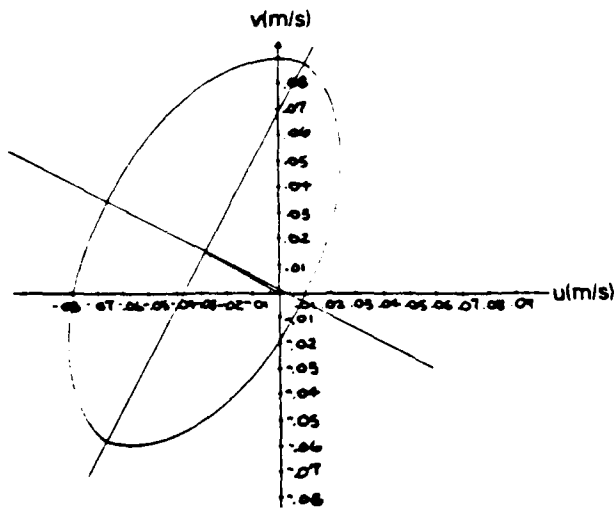
Free-Drift Error Vector
and Variance Ellipse
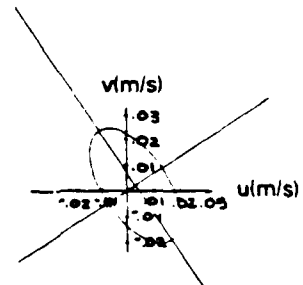
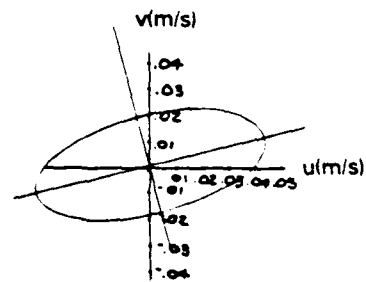Model Error Vector
and Variance Ellipse

Figure 5.9.   Ice Trajectory at Caribou During 27 January - 12 February 1976 (76RUN5C)

Figure 5.10.   Ice Trajectory at Station 17 During 27 January -
12 February 1976 (76RUN5C)

Trajectories

OBSERVED ——
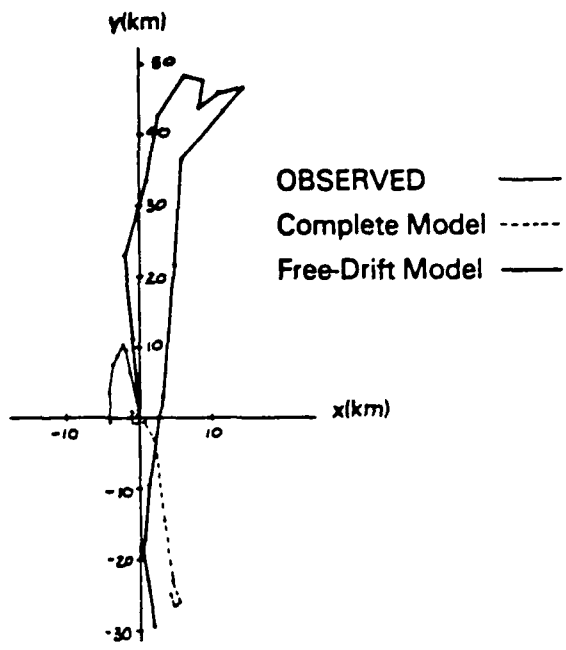Complete Model ------
Free-Drift Model ——

Free-Drift Error Vector
and Variance Ellipse
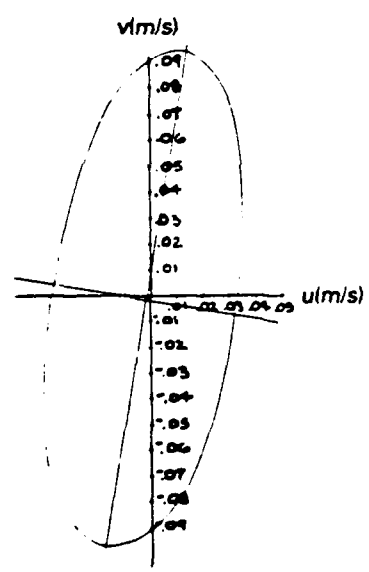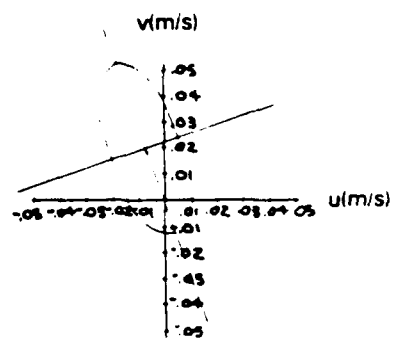
Model Error Vector
and Variance Ellipse

Figure 5.11.   Ice Trajectory at Station 20 During 27 January -
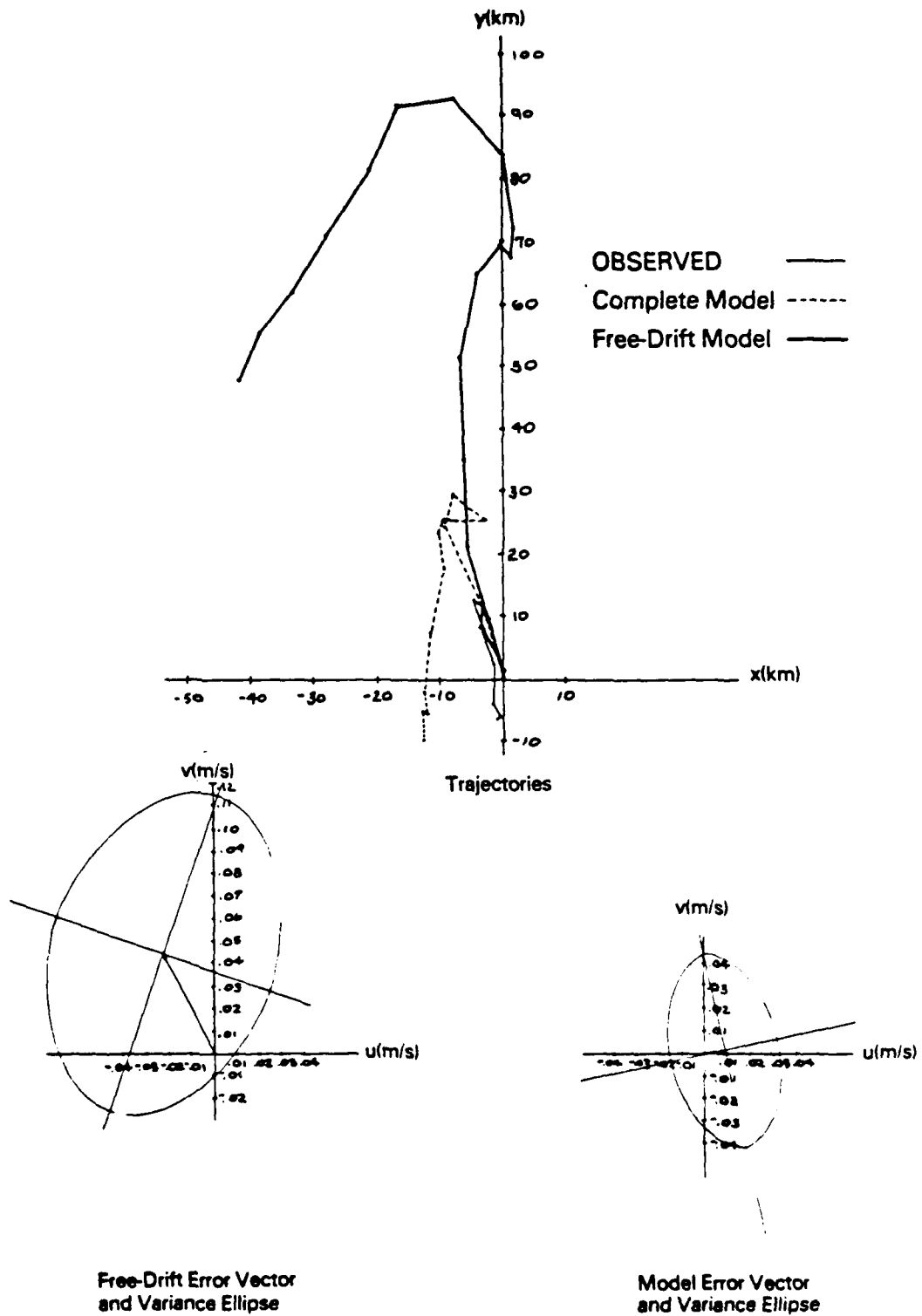12 February 1976 (76RUN5C)

Figure 5.12. Ice Trajectory at Station 16 During 27 January - 12 February 1976 (76RUN5C)

There are some interesting effects of geographic location on the complete ice dynamics model errors. The standard deviations given in Table 5.1 show that variances are consistently smallest in the central Arctic basin, largest in the transition zone and have intermediate values in the nearshore region. This is a consequence of the fixed boundary conditions at the shore. The model does best furthest removed from boundary constraints. As the fixed boundary begins to influence motions, the model does poorly because of the discontinuous nature of the transition region. In the nearshore area, the model still predicts some motion while the ice in fact moves hardly at all. While relative errors in this area may be large, the motions are small and the error vectors are thus not as large as in the transition region. The transition region between the fast nearshore ice and the pack ice is the most difficult in which to predict motions. This is a region of strong discontinuities in ice motion. In the stamukhi zone, shear ridging and shear leads are confined to narrow strips which are not resolved by the model. The region west of Banks Island frequently has large leads opening and closing, giving rise to large discontinuities in ice motion. It is interesting to note that the variance ellipses for these regions are consistently elongated parallel to the shoreline: east-west off Point Barrow and north-south off Banks Island (except for Station 17 which could be due to its location with respect to Amundsen Gulf). This is largely because large onshore motions are not possible.

5.2.4 June Through December 1975

This long-term free-drift calculation covers the period from late spring, when the ice is still fairly strong, through summer, when the ice has little strength (due to large fractions of open water) and free-drift is expected to work well, and into the fall when the ice regains its strength.

The observed positions of three manned camps are averaged and used to compute monthly ice velocity vectors. These are compared with monthly velocities from the free-drift model to compute error magnitudes and standard deviations (Thomas and Pritchard, 1979). The results are given

64

in Table 5.2. Error magnitudes are fairly uniform from June through December at about 0.01 m/s. The standard deviation on the other hand is significantly higher in November and December (0.06 to 0.07 m/s) than in the summer (0.03 m/s).

Table 5.2. LARGE-SCALE, MONTHLY, FREE-DRIFT ERROR MAGNITUDES, JUNE THROUGH DECEMBER 1975. (Thomas and Pritchard, 1979)

Error	June	July	Aug.	Sept.	Oct.	Nov.	Dec.
$|\bar{\varepsilon}|$ m/s	0.006	0.007	0.009	0.011	0.006	0.006	0.006
S_ε m/s	0.025	0.033	0.034	0.034	0.043	0.072	0.066

5.2.5 Twenty-Five Year Variability of Motions

As part of the research conducted for OCSEAP, a set of free-drift ice motions has been calculated on a monthly basis (Thomas and Pritchard, 1979). The input for these calculations was geostrophic winds based on 25 years of daily sea level pressures (1953-78) provided by the National Center for Atmospheric Research (Jenne, 1975). Free-drift motions were calculated monthly in the Beaufort and Chukchi seas by accumulating daily motions. For every month, these data were then averaged over the 25 years to give mean monthly motions and variance ellipses.

A typical variance ellipse has major and minor axes of 0.06 m/s and 0.02 m/s for a standard deviation of about 0.06 m/s. The smallest values occur in June and July with standard deviations as low as 0.03 m/s near Prudhoe Bay. The largest values are in the Chukchi Sea in November-February where one standard deviation may reach 0.09 m/s.

In the Beaufort Sea in May, the standard deviation of free-drift ice motions was ~0.04 m/s. This may be compared with a standard deviation of errors of 0.02 to 0.05 m/s from the free-drift calculations during 13-28 April 1975, 17-25 May 1975 and the June through October portion of the June through December 1975 free-drift calculations. An ice trajectory for 1 month calculated from the 25-year averaged ice motions will thus be about as accurate as a complete free-drift calculation for this time.

The situation is similar during the period from 27 January to 12 February 1976. The standard deviation from the free-drift calculation is about 0.10 m/s compared to expected variations from year to year of only 0.09 m/s.

Only the complete ice dynamics model gives a significant improvement over the 25-year average motions; the standard deviation drops to 0.036 m/s which is less than half of the variability in ice motions.

5.3 DISCUSSION

The ice drift models may now be evaluated in terms of their ability to predict daily ice trajectories. The accuracy of prediction is necessarily tied to the accuracy of the input winds and currents. Other errors arise when the model is inadequate, as when free-drift is assumed in winter. With the statistics assembled, it is possible to estimate how well the two models will perform at different times of year and what the influence of wind and current errors will be.

5.3.1 Effect of Errors in Input Winds and Currents

Ultimately, Coast Guard operations will require meaningful accumulated trajectory errors based on available wind and current data. It is not possible to assess errors in the winds and currents used to drive the models during the time periods of the AIDJEX experiment since this would require exact knowledge of the winds and currents everywhere. It is

66

interesting, however, to evaluate the wind and current errors necessary to produce the observed errors.

McPhee (1980) has shown that a free-drift model simulates ice drift accurately in the summer (July through mid-September). Errors in ice velocities may thus reasonably be ascribed to wind and current errors for this time. In Figure 5.13 mean velocity errors and standard deviations of errors for free-drift are plotted as a function of time of year. In the summer the mean daily velocity error is roughly 0.01 m/s (~1 km/day) with a standard deviation of 0.03 m/s (~3 km/day). For long-term free-drift, the ice velocity relative to geostrophic currents is essentially a linear function of the geostrophic wind speed U :

$$v - v_g = N_a^{\frac{1}{2}} U \tag{5.29}$$

where $N_a^{\frac{1}{2}} \simeq 0.014$. Thus, if U and $N_a^{\frac{1}{2}}$ are perfectly accurate, errors in ice velocity will equal errors in geostrophic current determinations. The geostrophic currents in the Beaufort Sea range from 0.01 to 0.03 m/s and are not well known (Hunkins, 1974). Highly energetic eddy currents with speeds up to 0.60 m/s and diameters of 10 to 20 km may further increase the variability in currents (Hunkins, 1980). Errors in geostrophic currents can thus entirely account for the errors and standard deviation of errors in ice velocity. Improvement of these errors is unlikely unless some better measure of dynamic topography of the Beaufort gyre becomes available.

Suppose instead that the geostrophic currents are perfectly known and that the wind is the only source of error. If $N_a^{\frac{1}{2}}$ is constant, then Equation (5.29) implies errors of 0.7 m/s in the geostrophic wind with a standard deviation of 2.1 m/s. Wind errors of about 2 m/s are not unusual; the mean geostrophic wind in summer is ~10 m/s (Albright, 1980), so this represents an error of only 20 percent. Independent measurements of geostrophic winds differ by about 13 percent. Such an error can account for a large part of the errors in ice velocity.
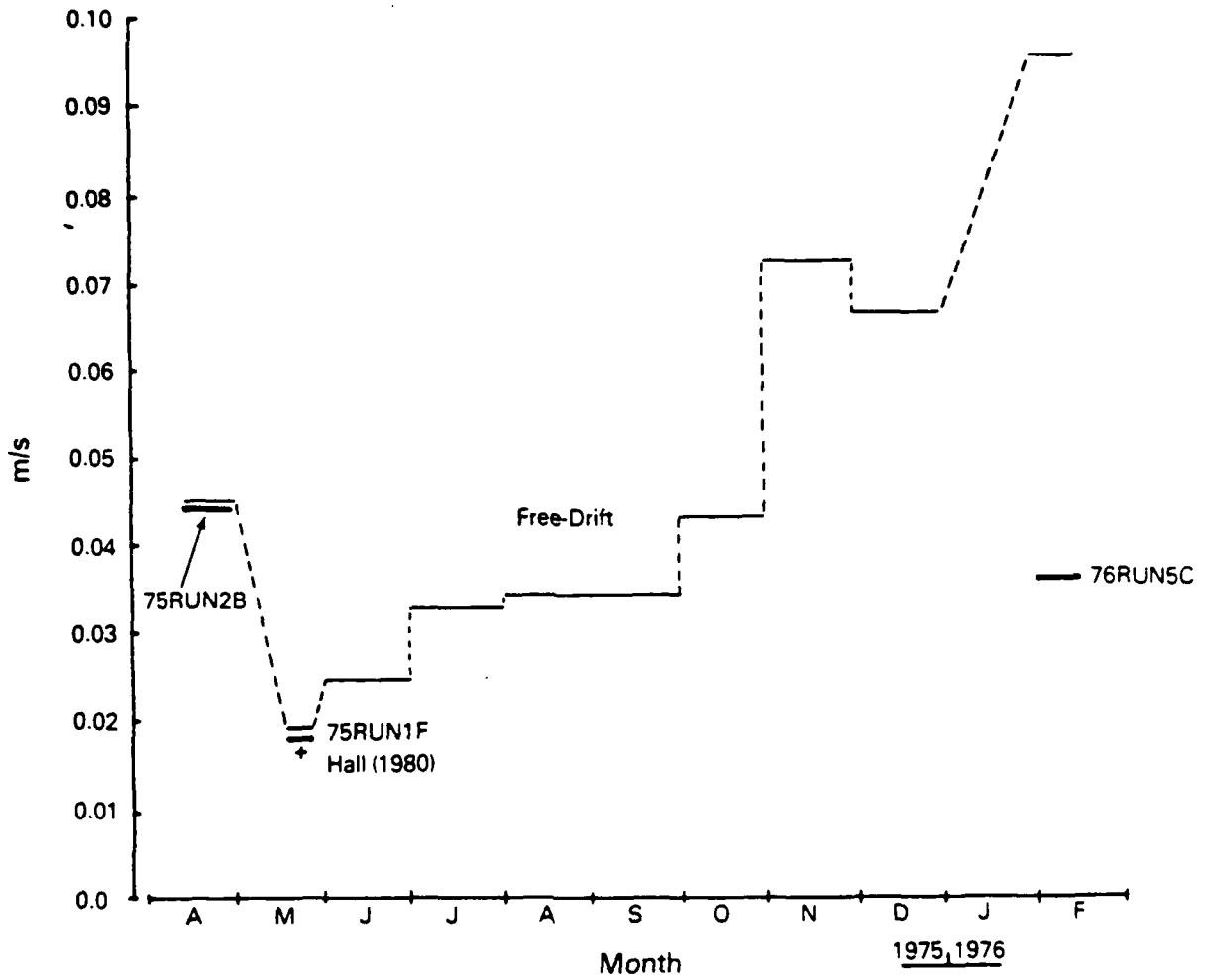
a. Standard Deviations of Errors
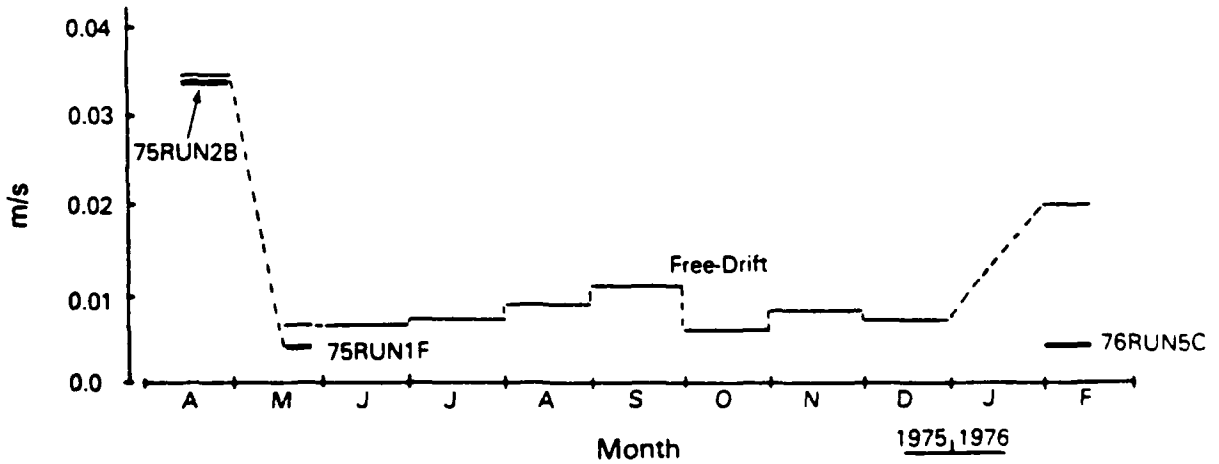
b. Mean Error Magnitudes

Figure 5.13. Mean Error Magnitudes and Standard Deviations as a Function of Time of Year

Denner and Ashim (1980) have analyzed errors between AIDJEX winds
and those produced by Fleet Numerical Weather Central (FNWC). For winds
greater than 5 m/s the mean error is ~40 percent. Variation of this
error is not given. Use of FNWC pressure maps to predict ice trajectories
should therefore give rise to errors 4 times as great as those produced
using AIDJEX pressure data.

The standard deviations calculated here may be used to predict
errors in future free-drift calculations. As seen in Figure 5.13, the
error magnitudes are uniformly much smaller than the standard deviations.
This leads to the possibility that these errors are not significantly
different from zero. The relevant statistic to check is $t_{n-1} = \frac{\sqrt{n} \, |\bar{\epsilon}|}{S}$
where n = number of days in comparison, $|\bar{\epsilon}|$ = average error magnitude
and S = standard deviation. If the error is 95 percent significant,
$t_{n-1} > t_{0.95,n-1}$ where $t_{0.95,n-1}$ is the students t-distribution
(Morrison, 1976, p. 367). For most of the calculations using the
free-drift model, the error is not significant. For 75RUN1F and 75RUN2B,
a significant error is apparent, but only for 75RUN2B is it unequivocal;
in fact, $t_{n-1}(75RUN2B) > t_{0.995,n-1}$.

5.3.2 Seasonal Variations in Performance

Ice conditions in the Arctic change considerably with season. We
expect to see this reflected in the performance of the two models
presented. Figure 5.13 shows the magnitudes and standard deviations of
velocity errors described in the previous sections as a function of time
of year. The error magnitudes of free-drift calculations appear to show
a minimum steady value of from 0.006 to 0.010 m/s from May through
December with larger errors for February and April. This might be
deceptive. The three calculations for February, April and May are made
from data sets of 10 to 15 days, while the calculations for June through
December include 30 days worth of data each. The central limit theorem
holds that the observed mean error should approach the true error magnitude
as the number of observations increases. Calculations based on short
time periods may thus be expected to estimate mean errors less accurately.

Nonetheless, we do know that the free-drift model should work better in the summer since the ice pack has essentially no strength at this time. The large errors in February and April reflect this fact.

Standard deviations of velocity errors show a much more pronounced seasonal effect which appears to be independent of sample size. The lowest values occur from May through September ranging from 0.019 to 0.035 m/s. The standard deviation increases in the fall to a maximum of 0.095 m/s in February and drops again in the spring. Mean wind speeds in the Arctic do not show a similar variation from season to season, so the increased variation in the winter is not due to increased wind input. Free-drift simply does not work well in the winter because the ice strength becomes appreciable at this time. When the ice strength is accounted for, by the complete ice dynamics model, the standard deviation in February drops to 0.036 m/s, which is comparable to the summer free-drift value.

5.3.3 Accumulating Errors in Trajectories

Over a period of days or weeks it is important to know how trajectory errors accumulate and how much variation can be expected in the errors. The trajectory error vector simply grows linearly with the number of days:

$$\underset{\sim}{\varepsilon}_t = N \overline{\underset{\sim}{\varepsilon}} \quad . \tag{5.30}$$

The variance also grows linearly as in a random walk:

$$S_t^2 = N S_\varepsilon^2 \tag{5.31}$$

where S_ε^2 is the variance of daily velocity errors. The standard deviation thus grows as the square root of N

$$S_t = \sqrt{N} \, S_\varepsilon \quad . \tag{5.32}$$

70

In practice, errors can accumulate in two ways, depending on whether the direction of the mean error is known reliably in addition to its magnitude. Figure 5.14 shows a schematic of a modeled ice trajectory. In this case, the mean daily error is assumed to be a known vector. The length of the predicted error vector grows linearly with the number of days in the model. Each circle represents one standard deviation in error magnitude; it encloses the area within which the probability of finding the true ice position is 0.683. The error is assumed to have a normal Gaussian distribution about its mean so radii of different probabilities may be easily found by solving

$$\text{erf} \left(\frac{r}{\sqrt{2} \ S_t} \right) = p(r) \tag{5.33}$$

for r where $p(r)$ is the desired probability.

In the context of searching for an oil spill whose trajectory has been predicted by the free-drift model, note that the area to be searched with a given probability of success increases linearly with time. If the direction of the error vector is unknown, the area to be searched increases substantially. The search area corresponds to an envelope about a set of circles of radius S_t whose centers lie on a circle of radius $|\underset{\sim}{\varepsilon}_t|$, Figure 5.15. These describe a circle of radius $r = |\underset{\sim}{\varepsilon}_t| + S_t$ to be searched. Since $|\underset{\sim}{\varepsilon}_t|$ increases linearly with time, the search area from this component of t increases as the square of time. This is a much more realistic situation since we do not have a good measure of mean error vectors averaged over long time periods. If these were available they could be used to correct the model, probably by correcting the geostrophic current, and the model would have a zero mean error. From Figure 5.13 it is apparent that a mean free-drift error magnitude of ~0.01 m/s is typical from May through December 1975. The standard deviation for this time period is about 0.03 m/s. After 7 days, this corresponds to a search radius of 13 km. After 1 month, the radius would be 46 km. This compares very favorably with the 25-year variability of motions which could locate an oil spill to within an ellipse 50 km wide by 150 km long. The area to be searched is thus about one-third that required if no trajectory is calculated.
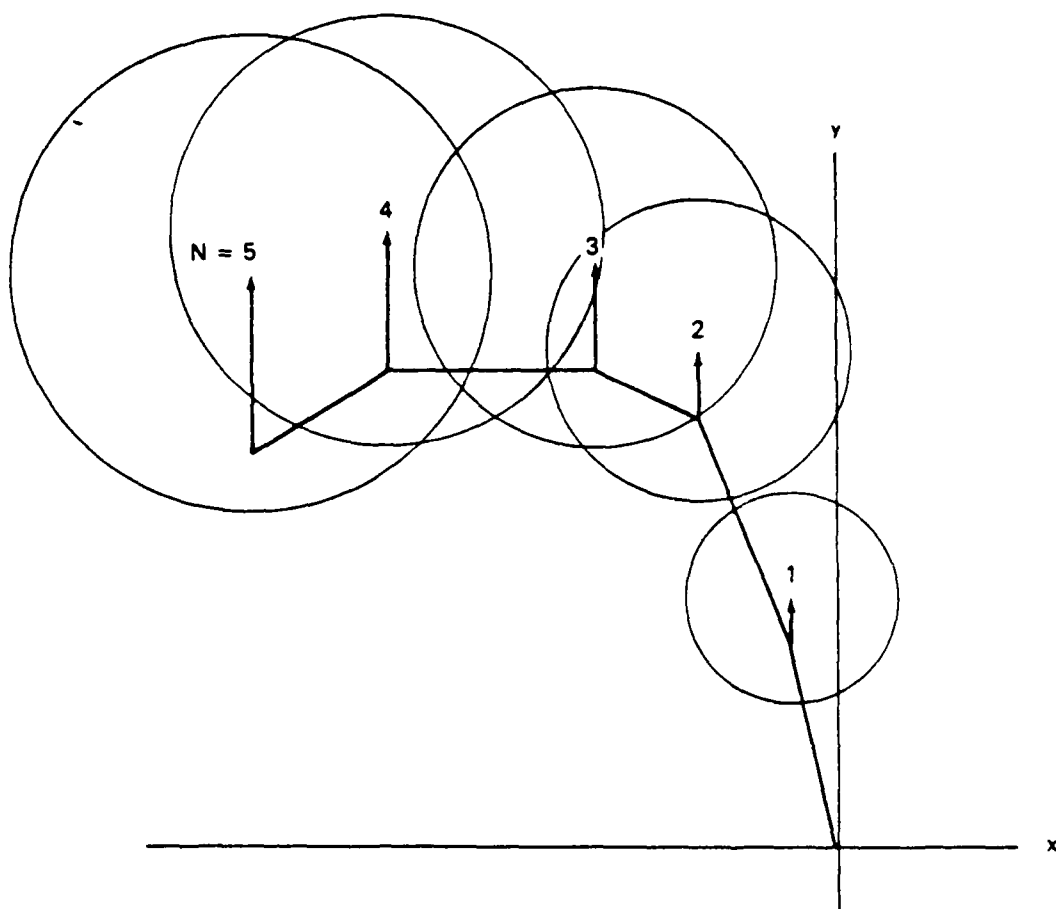
71

Figure 5.14. Accumulation of Errors in Trajectory when Mean Error Vector Is Known. Circles Represent the Area to Be Searched with a Probability of 0.683 of Finding the True Trajectory After N Days. Radii Are Given by $S_t = \sqrt{N} \; S_\varepsilon$. Error Vectors are Accumulated Mean Errors Given by $\varepsilon_t = N\bar{\varepsilon}$
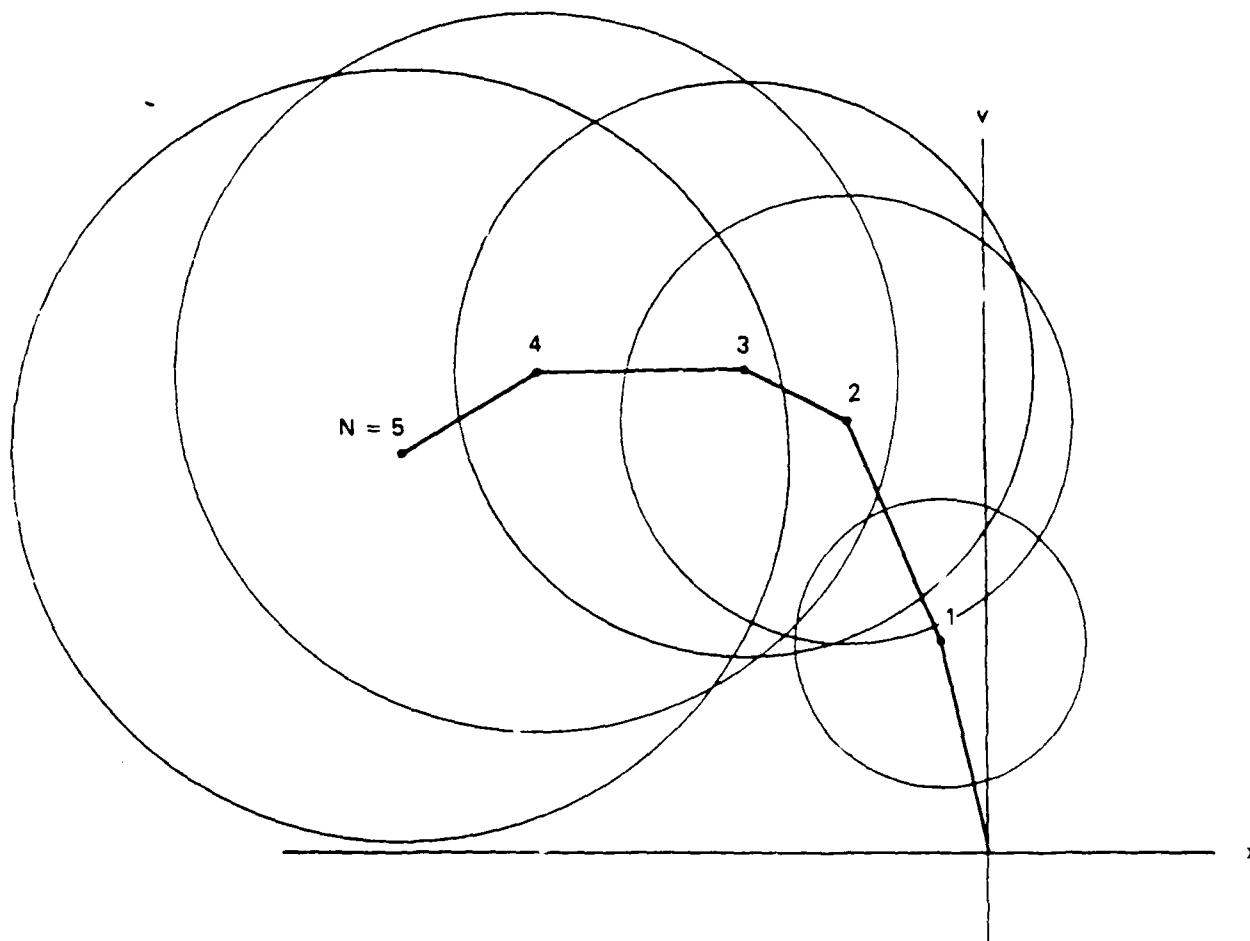
72

Figure 5.15. Accumulation of Errors in Trajectory if Only Error Magnitude and Standard Deviation Are Known. Circles Represent the Area to Be Searched with a Probability of 0.683 of Finding the True Trajectory After N Days. Radii Are Given by $|\varepsilon_t| + S_t$

From October to December 1975, the free-drift standard deviation doubles, but this does not cause a significant increase in the search radius since the mean error remains low. Assuming S_ε = 0.07 m/s and $|\bar{\varepsilon}|$ = 0.01 m/s gives a search radius of 68 km.

In the winter, the free-drift mean error can triple. Assuming a mean error of 0.03 m/s and a standard deviation of 0.07 m/s gives a search radius of 130 km which is comparable to the natural variability of motion. During this time, a free-drift calculation performs only a little better than assuming that the ice does not move at all.

The complete ice dynamics model, on the other hand, does quite well in the winter. If a mean error of 0.005 m/s and a standard deviation of 0.036 m/s are representative, this gives a search radius of only 35 km.

Chapter 6

RESOURCE REQUIREMENTS

6.1 GENERAL DISCUSSION

All calculations performed to date by the authors have used a
CDC 6400 computer. Resource requirements reflect this fact. If another
computer is used, then some of the requirements, central processing time
in particular, can change dramatically. The user can expect comparative
increases or decreases for both models. It should also be noted that
computation times and other resource requirements could be decreased
substantially by modifying the codes. This is especially true of the
complete ice dynamics model which has been coded to allow great flexibility
because it is a research tool, not an operational forecasting system.

Estimates of resource requirements are given separately for each
model. These estimates can be affected strongly by the format of input
data and by the format of the output and the printer/plotter device used
to present it. We assume that an operational forecasting system will
receive wind predictions from a U.S. governmental agency, such as the
NOAA National Weather Service or the Navy Fleet Numerical Oceanographic
Center, or the Canadian Atmospheric Environment Service in a form that
is immediately useful. A similar assumption is made for any ocean
current data that are available. Also, we assume that a line printer
and a plotter (either an x-y plotter or a CRT display with hard copies)
are available. Plotting software is also required to allow a concise
display of ice motion fields and trajectories. These requirements are
similar for both the free-drift and complete ice dynamics models.

6.2 FREE-DRIFT MODEL

6.2.1 Computer

The free-drift computer program determines the ice velocity at a
location independently of surrounding conditions. Therefore, except for

75

the need to have wind and current fields available, the trajectory of a given ice floe (a material point in the mathematical model) is found independently of surrounding locations. This fact implies that computer memory and timing requirements are minimal.

The computer program requires about 40 K octal words during compilation. Execution is estimated to require only a few thousand words, say 3 K octal. This does not include storage arrays for winds and currents. There are no requirements for mass storage units such as disks or tape drives.

Central processing unit timing requirements are roughly 3 ms per velocity estimate. There is no time step limitation, so free-drift velocity estimates can be made each 6 hours or whenever wind and current data are available. These execution costs are small enough to be considered negligible. Similarly, the peripheral processor and input/output times are negligible.

It is expected that the free-drift model could be executed on the smallest possible minicomputer, and probably on a hand-held programmable calculator. No attempts have been made to do so, however. It is important to be able to display ice trajectories on a CRT or x-y plotter to give confidence to the user. These plotting requirements overshadow actual needs for computing ice motions.

6.2.2 Manpower

An estimate of ice motion during one time increment requires initial position, average wind and current data and ice thickness. The manpower required to input these data and execute the computer program is too small to estimate accurately, whether the simulation is being performed for the first time or during an ongoing operation. Efforts to produce wind and current input have been considered separately, as have the plotting requirements. These manpower requirements will be dominated by the need to have personnel available full-time to calculate and interpret results.

6.3 COMPLETE ICE DYNAMICS MODEL

6.3.1 Computer

All simulations performed to date by the authors have used numerical grids roughly 12 x 15 cells in each direction, about 208 nodes. Such a grid can cover the Beaufort Sea with cells of about $\Delta = 40$ km . If the same region is covered with more cells of smaller sizes, then the computing time is proportional to Δ^{-3} . This occurs because the number of nodes is proportional to Δ^{-2} and the maximum time step is proportional to Δ . Thus, more cycles are needed to advance the solution the same increment in time.

The computer program requires approximately 100 K octal words during execution. This includes storage for both program, data and output arrays. Central memory is not increased appreciably if more cells are used because solutions are stored on disks or other mass storage units during computations. A disk (or other mass storage unit) is required to provide intermediate storage of solutions. Two time levels of solutions are stored simultaneously. Each solution describes about 26 variables for each mode. This is affected by the number of thickness levels used to describe the ice thickness distribution. A tape drive unit is used only as a backup for permanent file storage.

Central processing unit (CPU) timing requirements are roughly 20 ms per cell per cycle, exclusive of printout and plotting operations. This CPU time breaks down into about 14 percent for constitutive law, 35 percent for thickness distribution, 31 percent for momentum balance and the remaining 20 percent for array shifting and other overhead functions. Time steps are on the order of 3 minutes, so approximately 480 cycles are needed to increment the solution forward 1 day. This is the smallest time step used to date in all simulations. Peripheral processing times are observed to be about one-quarter to one-half of CPU times. Input/output times are observed to be about one-third to two-thirds of CPU times. This last estimate depends linearly on the frequency at which solutions are stored for later printing and plotting.

The computer resources required to execute the complete ice dynamics model can vary by a factor of 4 to 8, either longer or shorter depending on many specific parameters. A users' guide prepared by D. R. Thomas (unpublished manuscript) has indicated how such choices can affect timing. As an example of actual costs, the 17-day simulation of winter ice dynamics presented by Pritchard (1981) required approximately 22,600 CPU seconds to execute. The grid included 12 x 16 = 192 cells and a time step of 180 seconds per cycle was used. This time is about three-fourths of the average estimate presented in this section. For the sake of completeness, it is noted that known modifications could reduce this cost by an estimated factor of about 8, or to 12 percent of the stated cost.

6.3.2 Manpower

An individual simulation of sea ice dynamics using the complete model requires manpower to set up and initialize, to execute and to print or plot output and interpret results. The problem set up and initialization requires that a grid be selected and positions of all nodes be specified. Initial ice velocity, stress and thickness distribution are required throughout the region. Only the thickness distribution needs to be input with care at the beginning of a new simulation (or forecast). The grid, velocity and stress can be input once for any region of interest. Execution of the computer program typically is accomplished by a computer facility staff available as part of the computing cost. Plotting of output data and interpretation of results depend on the purpose of a simulation. If a basic understanding of ice dynamics in a new region or at a different time of year is needed, then interpretation of a simple month-long simulation is a two-to-four man-month effort. As a standard forecast, this postprocessing is minimal. For an operational forecasting system, manpower estimates are expected to be roughly comparable to free-drift model operations.

Chapter 7
CONCLUSION AND RECOMMENDATIONS

The free-drift model has been tested as a function of season and geographic location. Errors in free-drift calculations have been compared with the natural variability of ice motion and with the more sophisticated complete ice dynamics model.

The most significant error is the accumulated trajectory error. This determines the area to be searched (about the predicted position) after a given number of days for the true location of a point (oil spill) on the ice pack. After a month, the ice can move considerable distances (50 to 150 km) in the summer or winter. The free-drift model simulates a 1 month trajectory to within 50 km in the summer. Considering the low cost and ease of implementing the free-drift model, this represents a significant improvement over a search from the point of origin. In the winter, free-drift appears to offer, at best, only a marginal improvement over searching the historical variability ellipse. The complete ice dynamics model does much better in the winter and is comparable in accuracy to free-drift in the summer. This model is more difficult to implement, however, requiring tracking buoys on the perimeter of the area and accurate winds over the entire area. The free-drift model, in comparison, requires only local winds near the point of interest. The additional costs incurred in implementing the complete model must be weighed against the improvement in predicted motions.

Both the free-drift and the complete ice dynamics models would benefit substantially from an improved geostrophic current field in the Beaufort Sea. Such a current field, if accurately determined, could reduce mean daily errors to zero, though variability in errors would remain. Free-drift trajectory errors in the summer should fall to less than 20 km and in the winter, to less than 40 km. The free-drift model could easily be used to obtain the geostrophic current for any summer in which tracking buoy data are available. The ice velocity field given by the free-drift model is velocity relative to geostrophic current.

Monthly mean differences between modeled motions and observed motions
thus give the geostrophic current directly. These currents should vary
slowly over periods of months or longer and could also be used to
improve the accuracy of the complete ice dynamics model in the winter.
Accurate currents should reduce monthly complete model trajectory errors
in the winter to less than 20 km.

We recommend that the free-drift model be implemented to aid in
tracking oil spills from May until October and a complete ice dynamics
model be used during the winter and early spring months. The free-
drift model should also be used to construct a geostrophic current field
for the Beaufort Sea.

REFERENCES

Albright, M., "Geostrophic Wind Calculations for AIDJEX," _Sea Ice Processes and Models_, Edited by R. S. Pritchard, University of Washington Press, Seattle, pp. 402-409, 1980.

Brown, R. A., "The Resistance Law," _AIDJEX Bulletin No. 31_, University of Washington, Seattle, pp. 21-31, 1976.

Bugden, G. L., "The Deformation of Pack Ice by Ridging," _J. Geophys. Res._, _84_, pp. 1793-1795, 1979.

Coon, M. D., "Mechanical Behavior of Compacted Arctic Ice Floes," _J. Pet. Tech._, _257_, pp. 466-470, 1974.

Coon, M. D., " A Review of AIDJEX Modeling," _Sea Ice Processes and Models_, Edited by R. S. Pritchard, University of Washington Press, Seattle, pp. 12-33, 1980.

Coon, M. D., and R. S. Pritchard, "Mechanical Energy Considerations in Sea-Ice Dynamics," _J. Glac._, _24_(90), pp. 377-389, 1979.

Coon, M. D., G. A. Maykut, R. S. Pritchard, D. A. Rothrock and A. S. Thorndike, "Modeling the Pack Ice as an Elastic-Plastic Material," _AIDJEX Bulletin No. 24_, University of Washington, Seattle, pp. 1-105, 1974.

Coon, M. D., R. T. Hall and R. S. Pritchard, "Prediction of Arctic Ice Conditions for Operations," _Proceedings of Ninth Annual Offshore Technology Conference_, Houston, Texas, pp. 307-314, 1977.

Denner, W. W., and L. D. Ashim, "Operational Determination of Wind Stress on the Arctic Ice Pack," _Sea Ice Processes and Models_, Edited by R. S. Pritchard, University of Washington Press, Seattle, pp. 76-88, 1980.

Hall, R. T., "Seasonal Photo Mosaics of the AIDJEX Triangle," AIDJEX Bulletin No. 39, University of Washington, Seattle, pp. 79-84, 1978.

Hall, R. T., "A Test of the AIDJEX Ice Model Using Landsat Images," Sea Ice Processes and Models, Edited by R. S. Pritchard, University of Washington Press, Seattle, pp. 89-101, 1980.

Hunkins, K. L., "Subsurface Eddies in the Arctic Ocean," Deep-Sea Res., 21, pp. 1017-1033, 1974.

Hunkins, K. L., "Review of the AIDJEX Oceanographic Program," Sea Ice Processes and Models, Edited by R. S. Pritchard, University of Washington Press, Seattle, pp. 34-45, 1980.

Jenne, R. L., "Data Sets for Meteorological Research," NCAR Technical Note TN/1A-III, National Center for Atmospheric Research, Boulder, 1975.

Leavitt, E., "Surface-Based Air Stress Measurements Made During AIDJEX," Sea Ice Processes and Models, Edited by R. S. Pritchard, University of Washington Press, Seattle, pp. 419-429, 1980.

Leavitt, E., M. Albright and R. Baumann, "Variation in Planetary Boundary Layer Parameters Observed During AIDJEX," AIDJEX Bulletin No. 34, University of Washington, Seattle, pp. 149-163, 1978a.

Leavitt, E., M. Albright and F. Carsey, "Report on the AIDJEX Meterological Experiment," AIDJEX Bulletin No. 39, University of Washington, Seattle, pp. 121-147, 1978b.

McPhee, M. G., "Ice Ocean Momentum Transfer for the AIDJEX Ice Model," AIDJEX Bulletin No. 29, University of Washington, Seattle, pp. 93-111, 1975.

REFERENCES (Cont.)

M.꞉ee, M. G., "A Simulation of Inertial Oscillation ᵢn Drifting Pack
.. Ice," Dyn. Atmos. Ocean., 2, pp. 107-122, 1978.

McPhee, M. G., "An Analysis of Pack Ice Drift in Summer," Sea Ice Processes
and Models, Edited by R. S. Pritchard, University of Washington Press,
Seattle, pp. 62-75, 1980.

Morrison, D. F., Multivariate Statistical Methods, 2nd Ed., McGraw-Hill,
New York, 1976.

Nye, J. F., "A Coordinate System for Two-Dimensional Stress and Strain-
Rate and Its Application to the Deformation of Sea Ice," AIDJEX
Bulletin No. 33, University of Washington, Seattle, pp. 131-143,
1976.

Parmerter, R. R., and M. D. Coon, "A Model of Pressure Ridge Formation
in Sea Ice," J. Geophys. Res., 77, 00. 6565-6575, 1972.

Pritchard, R. S., "A Elastic-Plastic Constitutive Law for Sea Ice,"
J. Appl. Mech., 42(2), pp. 379-384, 1975.

Pritchard, R. S., "The Effect of Strength on Simulations of Sea Ice
Dynamics," Proceedings of the Fourth International Conference on
Port and Ocean Engineering under Arctic Conditions, Vol. 1,
Edited by D. B. Muggeridge, Memorial University of Newfoundland,
St. John's, pp. 494-505, 1978.

Pritchard, R. S., "A Simulation of Nearshore Winter Ice Dynamics in the
Beaufort Sea," Sea Ice Processes and Models, Edited by R. S. Prichard,
University of Washington Press, Seattle, pp. 49-61, 1980.

Pritchard, R. S., "Mechanical Behavior of Pack Ice," Mechanical Behaviour
of Structured Media, Edited by A. P. S. Selvadurai, Elsevier,
Amsterdam, 1981.

REFERENCES (Cont.)

Pritchard, R. S., and R. W. Reimer, "Ice Flow Through Straits" POAC 79,
Vol. 3, The University of Trondheim, Trondheim, pp. 61-74, 1979.

Pritchard, R. S., and D. R. Thomas, "The Range of Influence of Boundary
Parameters in the AIDJEX Model," Sea Ice Processes and Models,
Edited by R. S. Pritchard, University of Washington Press, Seattle,
pp. 113-123, 1980.

Pritchard, R. S., M. D. Coon and M. G. McPhee, "Simulation of Sea Ice
Dynamics During AIDJEX," Jour. Pressure Vessel Tech., 99(3),
pp. 491-497, 1977.

Pritchard, R. S., M. D. Coon and D. R. Thomas, "Modeling the Mechanical
Energy Budget of the Beaufort Sea Ice Cover," Flow Research
Report No. 137R, Flow Research Company, Kent, Washington,
pp. 51, 1979.

Reimer, R. W., R. S. Pritchard and M. D. Coon, "Beaufort and Chukchi
Sea Ice Motion, Part 2. Onset of Large Scale Chukchi Sea Ice
Breakout," Flow Research Report No. 133, Flow Research Company,
Kent, Washington, p. 92, 1979.

Rothrock, D. A., "The Energetics of the Plastic Deformation of Pack
Ice by Ridging," J. Geophys. Res., 80(33), pp. 4514-4519, 1975.

Rothrock, D. A., and R. T. Hall, "Testing the Redistribution of Sea Ice
Thickness from ERTS Photographs," AIDJEX Bulletin No. 29, University
of Washington, Seattle, pp. 1-19, 1975.

Thomas, D. R., "Behavior of Oil Spills Under Sea Ice - Prudhoe Bay,"
Flow Research Report No. 175, Flow Research Company, Kent, Washington,
December 1980.

REFERENCES (Cont.)

Thomas, D. R., and R. S. Pritchard, "Beaufort and Chukchi Sea Ice Motion,
 Part 1. Pack Ice Trajectories," Flow Research Report No. 133, Flow
 Research Company, Kent, Washington, 1979.

Thomas D. R., and R. S. Pritchard, "Beaufort Sea Ice Mechanical Energy
 Budget 1975-76," Flow Research Report No. 165, Flow Research Company,
 Kent, Washington, pp. 37, 1980.

Thorndike, A. S., and J. Y. Cheung, "AIDJEX Measurements of Sea Ice
 Motion 11 April 1975 to 14 May 1976," AIDJEX Bulletin No. 35,
 University of Washington, Seattle, pp. 1-149, 1977.

Thorndike, A. S., D. A. Rothrock, G. A. Maykut and R. Colony, "The
 Thickness Distribution of Sea Ice," Jour. Geophys. Res., 80,
 pp. 4501-4513, 1975.

Wadhams, P., and R. J. Horne "An Analysis of Ice Profiles Obtained
 by Submarine Sonar in the AIDJEX Area of the Beaufort Sea,"
 Technical Report 78-1, Scott Polar Research Institute, Cambridge,
 England, 1978.